### RESEARCH



# Dynamics of two mutually coupled thermoacoustic oscillators under external dual forcing

Chenjun Zhao · Liheng Zheng · Jie Zhou · Yu Guan

Received: 19 June 2025 / Revised: 31 July 2025 / Accepted: 6 August 2025 / Published online: 25 August 2025 © The Author(s) 2025

**Abstract** While non-resonant external forcing has proven effective in suppressing self-excited thermoacoustic oscillations in single oscillators, its application to systems consisting of multiple coupled oscillators remains poorly understood. This numerical study investigates external dual forcing for oscillation suppression in a system of two mutually coupled thermoacoustic oscillators, each modeled as a horizontal electrically heated Rijke tube. We demonstrate that symmetric dual forcing (equal energy distribution) achieves superior oscillation suppression, reducing global thermoacoustic amplitudes by up to 60% compared to single forcing at equivalent total energy. Spectral power analysis reveals that this enhancement arises from additional energy dissipation during inter-oscillator transfer under single forcing conditions. Furthermore, the control effectiveness can be enhanced—achieving an additional amplitude reduction of up to 5%—by carefully modulating the phase difference between the two forcing inputs. In contrast, detuning the forcing frequencies degrades suppression performance. These findings establish a theoretical basis for developing effective dual-forcing control strategies in coupled thermoacoustic systems and offer new insights into the underlying control mechanisms.

**Keywords** Thermoacoustic instability · Oscillation suppression · Forced synchronization · Reduced-order model

#### 1 Introduction

Thermoacoustic instability poses a critical concern in many power and propulsion systems due to its potential to degrade performance and efficiency, and even cause catastrophic structural damage [1-3]. In industrial systems featuring multiple combustors or flames, the nature of thermoacoustic instability becomes significantly more complex [4]. In such setups, the overall thermoacoustic behavior is shaped not solely by the flame-acoustic interaction within a single combustor, but by the collective dynamics of all combustors and any potential inter-combustor interactions. For example, can-annular combustors, which consist of multiple combustion-wise isolated chambers (cans) connected downstream by an annulus, display more intricate thermoacoustic behavior than a single-injector, single-chamber system [5]. This complexity arises because their thermoacoustic characteristics are governed by both flame-acoustic interactions within individual cans and acoustic-acoustic interactions across the cans. From the perspective of complex network and synchronization theory, this intricate problem can be

C. Zhao  $\cdot$  L. Zheng  $\cdot$  Y. Guan  $(\boxtimes)$ 

Department of Aeronautical and Aviation Engineering, The Hong Kong Polytechnic University, Kowloon, Hong Kong e-mail: yu.guan@polyu.edu.hk

L. Zheng · J. Zhou (⋈)

School of Aeronautics, Northwestern Polytechnical University, Xi'an 710072, China

e-mail: jiezhou@nwpu.edu.cn



investigated as a study of coupling-induced dynamics [6–8], such as mutual synchronization, within a ring-coupled network.

The synchronization framework has been widely adopted to study thermoacoustic instability in the past decade [9]. Mutual synchronization has attracted significant research interest, offering a valuable perspective for interpreting phenomena induced by interactions between self-excited thermoacoustic oscillators (TOs) and for modeling them using low-order canonical oscillators. For example, Jegal et al. [10] interpreted the global quenching phenomenon, triggered by coupling two self-excited lean-premixed combustors via a tube downstream of the combustor exit, as amplitude death, marking the first experimental evidence of such coupling-induced dynamics in reacting flow systems. Ghosh and Sujith [11], Ghosh et al. [12] studied the synchronization of coupled nonidentical oscillators, investigating the transition from chaos to order in dynamic systems and highlighting synchronization as a key mechanism for understanding complex systems, such as thermoacoustic instability in combustors. Subsequently, Guan et al. [13] and Liao et al. [14] employed van der Pol oscillators to numerically model various synchronization phenomena, including desynchronization due to quasiperiodicity, phase-locking, complete and partial amplitude death, and 2-can/pairwise/alternating anti-phase synchronization. These dynamics had been experimentally observed in prior studies of can-annular combustors by Moon et al. [15,16]. The study by Sahay et al. [17] indicates that when two thermoacoustic oscillators are simultaneously subjected to external forcing and coupling, the region of oscillation suppression is broader than when a single mechanism is used. Mondal et al. [18] research reveals the mechanisms of resonance amplification and asynchronous quenching, demonstrating how external forcing can effectively control the amplitude of thermoacoustic oscillations. Meanwhile, variations in the system's thermoacoustic amplitude have been investigated, motivated by passive control, under different coupling conditions and oscillator properties. For example, Coccolo et al. [19] studied the impact of fractional damping on the Duffing oscillator and found that fractional damping significantly alters the system's oscillation amplitude and asymptotic time, particularly under underdamped and overdamped conditions. A particular focus has been placed on triggering or amplifying the emergence of amplitude death in systems comprising multiple coupled self-excited TOs. For example, Ghosh et al. [20], Ghosh and Chakraborty [21] investigated the enlargement of amplitude death regions using the occasional coupling scheme. Their studies showed that the occasional coupling scheme, particularly the on-off coupling, expands the amplitude death regions when applied to delay-coupled oscillators like the Stuart-Landau and Rössler models, and thermoacoustic systems like the Rijke tube. This method proved to be more effective than continuous coupling, offering a practical means to suppress oscillations in systems where amplitude death is beneficial, such as in combustion or thermoacoustic oscillators. Thomas et al. [22,23] numerically investigated the effects of dissipative coupling, time-delay coupling, and external noise on the transition to amplitude death in a model system consisting of two mutually coupled Rijke tubes. Biwa et al. [24] as well as Hyodo and Biwa [25] experimentally examined how coupling types (e.g., dissipative coupling, timedelay coupling) and dimensions and numbers of coupling tubes affect the emergence of amplitude death using two connected electrically powered thermoacoustic engines. Zheng et al. [26] numerically demonstrated that amplitude death emerges in a larger parameter space when oscillators are arranged in a locally pairwise asymmetric pattern, and that increasing the number of adjacently coupled self-excited oscillators promotes its emergence. Extensive research on nonlinear dynamical systems-including studies on bifurcations [27–30], delayed feedback control [31,32], and fractional damping [19,33] also provides a conceptual foundation that can inspire new approaches to the analysis and control of thermoacoustic oscillations. Although the foregoing studies have offered valuable insights into stabilizing the overall system through adjustments to oscillator parameters and coupling conditions, the fixed geometry of the entire combustion system often limits the practical implementation of these modifications, rendering active control a more feasible solution.

Active control uses actuators to disrupt the energy feedback loop between flame and acoustic field and thus drive the system away from unstable states by adjusting key system parameters, which has been investigated for decades [34–36]. Among active approaches, open-loop control is particularly attractive for its simplicity and independence from the system's temporal behavior, as it does not require real-time feedback from



sensors or the use of complex control algorithms. By applying forcing at a non-resonant frequency, the initial energy feedback loop can be effectively disrupted, resulting in a substantial reduction of thermoacoustic amplitude [37–41]. Furthermore, this method is effective not only for suppressing limit-cycle oscillations but also for mitigating highly nonlinear quasiperiodic and chaotic oscillations [42,43]. This versatility paves the way for a unified control configuration capable of flexibly addressing various types of thermoacoustic oscillations. While open-loop control has been extensively studied in single combustor systems, its effectiveness-and its potential synergy with acoustic coupling-remains poorly understood in multicombustor configurations such as can-annular combustors. In these systems, the additional complexity introduced by acoustic coupling between cans, which enables acoustic wave propagation not only to neighboring cans but also to remote ones via the annular pathways, presents significant challenges for designing effective forcing strategies. Sahay et al. [17] observed that in a coupled thermoacoustic system with both mutual coupling and asymmetric forcing (under single forcing), oscillation quenching can occur over a broader parametric range than in cases where either coupling or forcing is applied alone. This finding motivates further investigation into whether dual forcing involving multiple actuators—offers advantages over single forcing in such configurations, particularly when coupling conditions are insufficient to trigger amplitude death.

Building on aforementioned findings and concerns, three key research questions are addressed in this study: (1) Will dual forcing outperform single forcing when suppressing thermoacoustic oscillations in a system consisting of two mutually coupled self-excited TOs? (2) What are the optimal forcing conditions to achieve maximum thermoacoustic oscillation suppression? (3) If dual forcing outperforms single forcing, what is the underlying mechanism behind this superior performance? We aim to answer these three research questions for the following reasons. First, when dealing with a complex system comprising multiple TOs that are mutually coupled, the optimal deployment and distribution of forcing energy remain open questions. While open-loop control has proven effective in suppressing self-excited oscillations in a single TO, it remains uncertain whether simply replicating this strategy in systems with multiple, mutually coupled TOs will yield similar results. The inherent time delay associated with the propagation of forcing-induced disturbances between TOs further complicates the simultaneous fulfillment of optimal forcing conditions across the system—and may even degrade control performance. In contrast, using independent forcing inputs introduces greater flexibility, enabling the tuning of amplitudes, frequencies, and phase delays between the inputs. This enhanced controllability may prove more effective in managing thermoacoustic oscillations in such complex, interconnected systems, thereby improving the adaptability and robustness of the control strategy.

To answer these key research questions, we establish a model system consisting of two mutually coupled Rijke tubes and investigate its response to external dual forcing under various conditions. By systematically varying key forcing parameters—including forcing amplitude ratio, total forcing amplitude, and phase delay and frequency detuning between the two forcing inputs—we aim to clarify their effects on the thermoacoustic amplitude of both individual oscillators and the overall system. This analysis seeks to identify the optimal forcing conditions for maximum oscillation suppression and to elucidate the underlying suppression mechanisms from the perspective of spectral power variation. The paper is organized as follows. In Sect. 2, we describe the model and define the non-dimensional parameters. In Sect. 3, we investigate the control effects of the forcing amplitude ratio, total forcing amplitude, and phase delay and frequency detuning between the two forcing inputs. This is achieved by comparing the responses of both individual oscillators and the overall system under dual forcing and single forcing. Finally, we summarize our findings and present the conclusion of this study in Sect. 4.

### 2 Mathematical model

We first develop a generic coupled thermoacoustic model system by mutually coupling two horizontal Rijke tubes, accounting for open boundary conditions, negligible mean flow, spatial variations in average temperature within the tubes, and natural convection in the ducts. The Rijke tube model has been widely employed in previous studies to investigate the nonlinear dynamics of thermoacoustic systems [44–47].



Linearized momentum and energy equations can be derived as follows:

$$\tilde{\rho}\frac{\partial \tilde{u}'}{\partial \tilde{t}} + \frac{\partial \tilde{p}'}{\partial \tilde{x}} = 0,\tag{1}$$

$$\frac{\partial \tilde{p}'}{\partial \tilde{t}} + \gamma \bar{p} \frac{\partial \tilde{u}'}{\partial \tilde{x}} + \zeta \tilde{p}' = (\gamma - 1) \dot{\tilde{Q}}' \delta(\tilde{x} - \tilde{x}_f). \tag{2}$$

In this study, symbols with a superscript ( ) represent dimensional variables, while those with a superscript ( ) denote fluctuating variables. Specifically,  $\tilde{t}$ ,  $\tilde{u}$ , and  $\tilde{p}$  represent time, acoustic velocity, and acoustic pressure in the duct, respectively. The symbol  $\tilde{x}$  refers to the distance along the inlet of the duct, with  $\tilde{x}_f$  being the position of the heat source. The chosen value for  $\tilde{x}_f = 0.25L$  is optimal for producing self-excited thermoacoustic oscillations in the duct. The parameters  $\tilde{\rho}$ ,  $\gamma$ ,  $\zeta$ , and  $\tilde{Q}'$  represent the density, specific heat ratio, damping coefficient, and heat release rate in the duct, respectively. The function  $\delta()$  is the Dirac delta function, used to define the compactness of the heat source. The boundary condition at  $\tilde{x} = L$  (where L is the duct length) is  $\tilde{p}'|_{\tilde{x}=L} = 0$ , which implies that the pressure fluctuation  $\tilde{p}^{T}$  is negligible at both duct ends. To simplify the analysis, the variables in Eqs. (1) and (2) are considered in their non-dimensional form:

$$x = \frac{\tilde{x}}{L}, \quad t = \frac{\tilde{t}c_0}{L}, \quad u' = \frac{\tilde{u}'}{u_0},$$

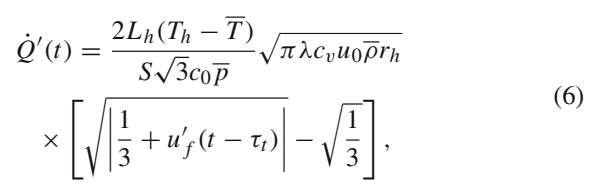
$$p' = \frac{\tilde{p}'}{p}, \quad \dot{Q}' = \frac{\dot{\tilde{Q}}'}{c_0 \bar{p}}, \quad M = \frac{u_0}{c_0},$$
(3)

where  $c_0$ ,  $u_0$ ,  $\bar{p}$ , and M are the sound speed, mean flow velocity, pressure, and Mach number, respectively. Equations (1) and (2) can be transformed into their non-dimensional forms using Eqs. (3):

$$\gamma M \frac{\partial u'}{\partial t} + \frac{\partial p'}{\partial x} = 0, \tag{4}$$

$$\frac{\partial p'}{\partial t} + \gamma M \frac{\partial u'}{\partial x} + \zeta p' = (\gamma - 1) \dot{Q}' \delta(x - x_f). \tag{5}$$

The heat release,  $\dot{Q}'$ , is modeled using a modified form of King's law [48,49], which relates the quasisteady heat transfer from a heated cylinder to the surrounding flow. The modified King's law primarily captures the amplitude-limiting effect of nonlinearity on acoustic growth. It is expressed as follows:



where  $L_h$ ,  $T_h$ , and  $r_h$  are the length, temperature, and radius of the heater wire, respectively.  $\overline{T}$  is the average temperature of the surrounding air. S is the cross-sectional area of the duct.  $\lambda$  and  $c_v$  are the thermal conductivity and constant-volume specific heat, respectively.  $\tau_t$  is the response time lag between the start of the heat source's response to the acoustic velocity perturbation,  $u_f'$ , due to the thermal inertia of the heater wire

To solve Eqs. (4) and (5), we apply the Galerkin method to convert the partial differential equations into a series of ordinary differential equations. To achieve this, we represent the dimensionless velocity u' and the pressure fluctuation p' as orthogonal functions that satisfy the boundary conditions [50,51]:

$$u' = \sum_{j=1}^{N} \eta_j \cos(j\pi x), \tag{7}$$

$$p' = -\sum_{j=1}^{N} \dot{\eta_j} \frac{\gamma M}{j\pi} \sin(j\pi x), \tag{8}$$

where  $\eta_j$  and  $\dot{\eta}_j$  refer to the time-dependent coefficients associated with the *j*th mode of the acoustic velocity u' and pressure fluctuation p', respectively. The symbol N denotes the total number of Galerkin modes considered in the analysis. The convergence of Galerkin truncation is validated in Appendix A. We choose N=5 to balance accuracy and computational efficiency.

By solving the following set of ordinary differential equations, we obtain the temporal evolution of a single Rijke tube:

$$\frac{\mathrm{d}\eta_j}{\mathrm{d}t} = \dot{\eta_j},\tag{9}$$

$$\frac{\mathrm{d}\dot{\eta}_{j}}{\mathrm{d}t} + 2\zeta_{j}\omega_{j}\dot{\eta}_{j} + \omega_{j}^{2}\eta_{j}$$

$$= -j\pi K \left[ \sqrt{\frac{1}{3} + u_{f}'(t - \tau_{t})} - \sqrt{\frac{1}{3}} \right] \sin(j\pi x_{f}), \tag{10}$$



where  $\omega_j = j\pi$  denotes the angular frequency of the jth Galerkin mode. The thermal inertia of heat transfer in the medium is modeled using a time lag parameter,  $\tau_t$ . The acoustic damping coefficient,  $\zeta_j$ , developed by Matyeev [52] is defined:

$$\zeta_j = \frac{1}{2\pi} \left[ c_1 \frac{\omega_j}{\omega_1} + c_2 \sqrt{\frac{\omega_1}{\omega_j}} \right],\tag{11}$$

where the damping coefficients  $c_1$  and  $c_2$  are specified. In this study, we set  $c_1 = 0.1$ ,  $c_2 = 0.06$ ,  $\tau_t = 0.25$ , M = 0.005, and  $x_f = 0.25$  for the Rijke tube. As for the non-dimensional heater power K, it is defined:

$$K = 4(\gamma - 1) \frac{2L_h(T_h - \overline{T})}{M\gamma S\sqrt{3}c_0\overline{p}} \sqrt{\pi\lambda c_v u_0\overline{\rho} r_h}, \qquad (12)$$

where K=2 is selected to ensure that the two self-excited TOs operate sufficiently far from the bifurcation point (around K=0.6). The numerical scheme of solving this self-excited oscillator is validated as shown in Appendix A.

In this study, the two self-excited TOs, referred to as TO1 and TO2, are coupled via dissipative and time-delay coupling terms, following the approach used in previous studies on generic coupled thermoacoustic systems [22,26,47]. The dissipative coupling represents interactions where the propagation time between oscillators is negligible compared to the oscillation period. While the time-delay coupling accounts for interactions where finite propagation time plays a critical role in the feedback. Each oscillator is independently subjected to a sinusoidal forcing. We use the subscripts "1" and "2" to denote parameters or variables of TO1 and TO2, respectively. This coupled thermoacoustic model system, under dual forcing, is modeled as follows:

$$\frac{\mathrm{d}\eta_{1,j}}{\mathrm{d}t} = \dot{\eta}_{1,j},\tag{13}$$

$$\frac{\mathrm{d}\dot{\eta}_{1,j}}{\mathrm{d}t} + 2\xi_{j}\omega_{j}\dot{\eta}_{1,j} + \omega_{j}^{2}\eta_{1,j}$$

$$= -j\pi K \left[ \sqrt{\left| \frac{1}{3} + u'_{f,1}(t - \tau_{t}) \right|} - \sqrt{\frac{1}{3}} \right]$$

$$\sin\left(j\pi x_{f}\right) + \underbrace{k_{d}\left(\dot{\eta}_{2,j} - \dot{\eta}_{1,j}\right)}_{\text{dissipative coupling}}$$

$$+\underbrace{k_{\tau} \left( \dot{\eta}_{2,j}(t - \tau_{\text{tube}}) - \dot{\eta}_{1,j}(t) \right)}_{\text{time-delay coupling}}$$

$$+\underbrace{A_{1} \sin(2\pi f_{f,1}t),}_{\text{forcing term}}$$
(14)

and

$$\frac{\mathrm{d}\eta_{2,j}}{\mathrm{d}t} = \dot{\eta}_{2,j},\tag{15}$$

$$\frac{\mathrm{d}\dot{\eta}_{2,j}}{\mathrm{d}t} + 2\xi_{j}\omega_{j}\dot{\eta}_{2,j} + \omega_{j}^{2}\eta_{2,j}$$

$$= -j\pi K \left[ \sqrt{\left| \frac{1}{3} + u'_{f,2}(t - \tau_{t}) \right|} - \sqrt{\frac{1}{3}} \right]$$

$$\sin\left(j\pi x_{f}\right) + \underbrace{k_{d}\left(\dot{\eta}_{1,j} - \dot{\eta}_{2,j}\right)}_{\text{dissipative coupling}}$$

$$+ \underbrace{k_{\tau}\left(\dot{\eta}_{1,j}(t - \tau_{\text{tube}}) - \dot{\eta}_{2,j}(t)\right)}_{\text{time-delay coupling}}$$

$$+ \underbrace{A_{2} \sin(2\pi f_{f,2}t),}_{\text{forcing term}} \tag{16}$$

where the coupling parameters are set as  $k_d=1.0$ ,  $k_\tau=0.2$ , and  $\tau_{\rm tube}=0.4$ , under which the overall thermoacoustic amplitude of the coupled system (0.01) is lower than that of the uncoupled oscillators (0.02), due to the influence of time-delay coupling. We focus on this scenario because (i) the TOs are nominally identical under ideal design conditions where amplitude death hardly emerges (amplitude death requires a frequency detuning between TOs), and (ii) our primary objective is to examine the role of external forcing in suppressing oscillations.

# 3 Results and discussions

Before evaluating the potential for enhanced performance of oscillation suppression in the coupled thermoacoustic system using dual forcing, we first define several non-dimensional parameters. The total forcing amplitude is given by  $\alpha = \sqrt{A_1^2 + A_2^2}$ , where  $A_1$  and  $A_2$  are the forcing amplitudes applied to the two TOs. The forcing amplitude ratio is defined as  $\beta = A_2/A_1$ , where  $\beta = 1$  corresponds to symmetric dual forcing, and  $\beta \neq 1$  corresponds to asymmetric dual forcing. The special case of  $\beta = 0$  corresponds to single forcing



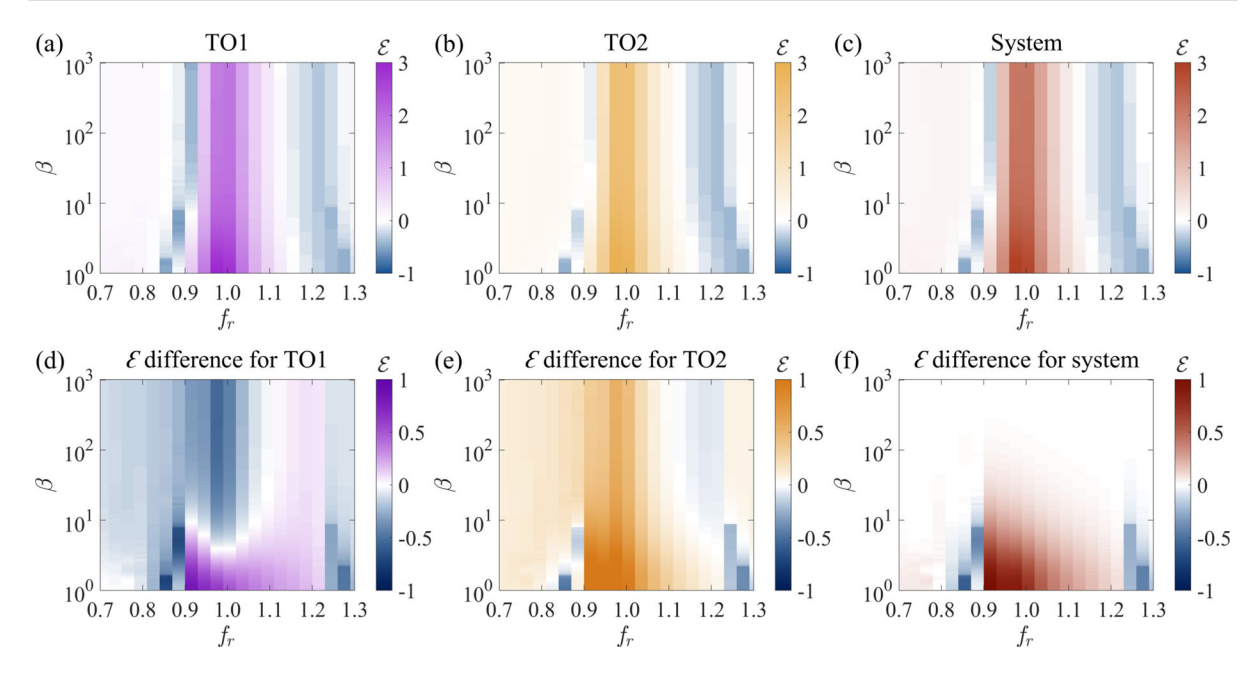


**Fig. 1** From left to right, forced responses ( $\mathcal{E}$ ) of TO1, TO2, and the overall system are shown in the top row, and their differences in  $\mathcal{E}$  between dual forcing and single forcing (the forcing is only applied to TO1 and  $\beta=0$ ) are shown in the bottom row. In all panels, purple, yellow, and red regions indicate oscillation amplification due to forcing. In contrast, blue regions indicate

oscillation suppression due to forcing. The remaining regions suggest that  $\mathbf{a} - \mathbf{c}$  the system hardly responds to forcing or that  $\mathbf{d} - \mathbf{f}$  dual forcing offers no significant advantage over single forcing in terms of oscillation suppression.  $\alpha$  is fixed to 4 for all cases. (Color figure online)

applied only to TO1. The non-dimensionalized forcing frequencies are defined as  $f_{r,1} \equiv f_{f,1}/f_{n,1}$  and  $f_{r,2} \equiv f_{f,2}/f_{n,2}$ , respectively.  $f_{n,1}$  and  $f_{n,2}$  are the natural frequencies of two TOs. Since the chosen values for the parameters of two TOs are the same and they are in-phase synchronized after coupling,  $f_{n,1} = f_{n,2} =$  $f_n$ , and we use  $f_r$  to denote the non-dimensionalized forcing frequency. To quantify the effectiveness of dual forcing, we introduce a non-dimensional parameter  $\mathcal{E} \equiv (p'_{f,\text{RMS}} - p'_{0,\text{RMS}})/p'_{0,\text{RMS}}$ , where  $p'_{f,\text{RMS}}$  and  $p'_{0.RMS}$  are the root mean square (RMS) of the pressure fluctuations under forced and unforced conditions, respectively. A negative value of  $\mathcal{E}$  indicates oscillation suppression (i.e., forcing works to suppress oscillations), while a positive value indicates amplitude amplification (i.e., forcing does not work and deteriorates the scenario).

# 3.1 Forcing amplitude ratio $\beta$

We first investigate how the coupled system's response to dual forcing varies within a parameter space defined by  $\beta$  and  $f_r$ . For each examined parameter space,  $\alpha$  is held constant. Since the influence of  $\beta$  and  $f_r$  on the coupled system's response becomes sufficiently significant when  $\alpha$  is large, we show one map ( $\alpha = 4$ ) here and put results of other  $\alpha$  values (0.9, 1, 2, and 3) in Appendix B in order to keep the flow of this paper concise. In each figure, the top row (from left to right) shows the forced responses of TO1, TO2, and the overall system. The bottom row (from left to right) shows the difference in the non-dimensional parameter  $\mathcal{E}$  between dual forcing and single forcing. Purple, vellow, and red regions indicate oscillation amplification due to forcing. In contrast, blue regions indicate oscillation suppression due to forcing. The remaining regions suggest that the system hardly responds to forcing or that dual forcing offers no significant advantage over single forcing in terms of oscillation suppression.

Noticeable blue regions appear not only in the top row of Fig. 1, demonstrating that dual forcing effectively weakens thermoacoustic oscillations in the system, but also in the bottom row, indicating that dual forcing outperforms single forcing in suppressing ther-



moacoustic oscillations. As  $\alpha$  increases from 0.9 to 4, the blue regions expand and deepen in color, consistent with previous studies on forced synchronization [18,53], which showed that higher forcing amplitudes ( $\alpha$  in this study)—approaching the critical threshold for synchronization—can induce oscillation suppression via asynchronous quenching. We will later show in Sect. 3.3 that the spectral power of  $f_n$  mode is weakened linearly as a function of the forcing amplitude  $A^2$ , which agrees with previous observations of asynchronous quenching [54,55]. The increasingly pronounced amplitude amplification near  $f_r = 1$  is also a characteristic phenomenon in forced synchronization. Additionally, we identify an interval of  $\beta$  values that yield improved oscillation suppression. These  $\beta$  values fall within the range  $10^{0}$ – $10^{0.7}$ , leading to especially prominent oscillation suppression when  $f_r$  is around 0.85 and 1.25 (see Fig. 1d-f). Meanwhile, it is worth noting that this behavior differs from the oscillation suppression observed near  $f_r = 1$ , which primarily results from the redistribution of forcing energy from TO1 to TO2—i.e., a significantly larger  $A_2$  than  $A_1$ at higher  $\beta$  values. Consequently, oscillation suppression near  $f_r = 1$  is observed only in TO1 and not in the forced response of the overall system. In contrast, the reductions observed near  $f_r = 0.85$  and 1.25 are evident in the overall system response, confirming that dual forcing achieves superior suppression compared to single forcing.

In a quick summary, we have demonstrated that by approximately equally distributing the forcing energy, there exist specific regions in the  $\beta$ - $f_r$  parameter space where dual forcing outperforms single forcing in this coupled thermoacoustic system. The values of  $\beta$  associated with enhanced suppression are predominantly within the range of  $10^0$  to  $10^{0.7}$ , while the corresponding normalized forcing frequencies  $f_r$  are centered around 0.85 and 1.25.

### 3.2 Total forcing amplitude $\alpha$

In the previous section, we observed that dual forcing outperforms single forcing when  $\beta$  lies within the range of  $10^0$  to  $10^{0.7}$ . This initial observation was based on a coarse sweep over the parameter  $\alpha$ . Notably,  $\alpha$  plays a crucial role in oscillation suppression, as it determines the total forcing energy applied in the control process. To assess whether this trend persists over a broader

parameter space-and to more thoroughly examine the role of  $\alpha$ , we conducted a comprehensive search for the global maximum oscillation suppression. The search spans  $\alpha$  from 0.5 to 8 (step size 0.1),  $\beta$  from 10<sup>0</sup> to  $10^3$  (exponent step size 0.01), and  $f_r$  from 0.70 to 1.30 (step size 0.02). These ranges were selected based on two main considerations: (1) ensuring  $\alpha$  is sufficiently large to achieve oscillation suppression even when the non-resonant forcing frequency significantly deviates from the natural frequency (i.e.,  $f_r \gg 1$  or  $\ll$  1), and (2) extending  $\beta$  to values where dual forcing begins to approximate single forcing (i.e.,  $A_2/A_1$ becomes very large). The optimal oscillation suppression,  $\mathcal{E} = -0.47$ , occurs at  $\beta = 1$  (10<sup>0</sup>),  $\alpha = 4.7$ , and  $f_r = 1.30$ , consistent with our preliminary findings in Sect. 3.1, as  $\beta$  remains within the previously identified effective range. This result suggests that dual forcing is most effective when the forcing energy is evenly distributed between the two sources. Based on this insight, we fix  $\beta = 1$  in the subsequent analysis to isolate the influence of varying  $\alpha$  on the system's response, as shown in Fig. 2.

As shown in Fig. 2a, a central inverted triangular region, where the system's response is significantly amplified, is flanked by two blue triangular bands indicating a reduced overall response. This pattern of  $\mathcal{E}$  variation resembles the classical Arnold tongue observed in forced synchronization of a single TO under single forcing [56]. In such a classical scenario of forced synchronization, two oscillation suppression zones typically emerge on either side of the Arnold tongue due to asynchronous quenching [56]. The loci of maximum oscillation suppression, marked by circular symbols at each  $f_r$ , delineate a  $\vee$ -shaped boundary corresponding to the synchronization boundary beyond which the system is forced to oscillate at the forcing frequency [56]. These characteristic features of forced synchronization are also evident in the coupled system under single forcing (applied to TO1), as shown in Fig. 2b. The difference in  $\mathcal{E}$  between dual forcing and single forcing, illustrated in Fig. 2c, displays a similar pattern to that in Fig. 2a. The central region on the left half of Fig. 2c is predominantly deep red, indicating that dual forcing, in this regime, amplifies the responsei.e., it is less effective at suppressing oscillations. In contrast, two narrower blue bands appear where dual forcing outperforms single forcing. When  $f_r = 0.86$ and  $\alpha = 3.7$ , around 60% more amplitude reduction can be achieved using dual forcing than using single forc-



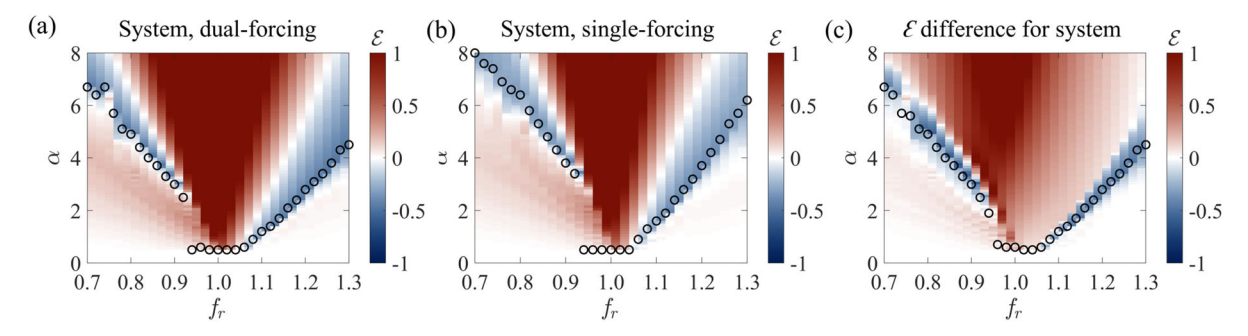


Fig. 2 Forced responses  $(\mathcal{E})$  of the system under **a** dual forcing and **b** single forcing, with the loci of maximum oscillation suppression, marked by circular symbols at each  $f_r$ . **c** Difference

in  $\mathcal{E}$  between dual forcing and single forcing, with the loci of dual forcing outperforming single forcing the most, marked by circular symbols at each  $f_r$ 

ing. Notably, the loci of maximum  $\mathcal{E}$  difference align closely with the loci of maximum oscillation suppression in Fig. 2a. However, the blue bands indicative of improved performance of dual forcing are considerably narrower than the oscillation suppression regions in Fig. 2a. This is primarily because, for a given forcing frequency  $f_r$ , dual forcing achieves the maximum oscillation suppression at a lower total forcing amplitude compared to single forcing (i.e.,  $\alpha^* < A_1^*$ , where  $\alpha^*$  and  $A_1^*$  denote the critical amplitudes for using dual forcing and single forcing, respectively). This difference is reflected in the openness of the ∨-shaped blue regions: the Arnold tongue of single forcing case is narrower, while that of dual forcing case is broader. Although similar levels of oscillation suppression can be achieved by increasing  $A_1$  further in single forcing as shown in Fig. 2b, the higher energy requirement makes it less efficient. This energy inefficiency is a key reason why dual forcing ultimately outperforms single forcing—a point that will be elaborated in the following section.

# 3.3 Why does dual forcing outperform single forcing?

In this section, we aim to provide a mechanistic interpretation of why dual forcing outperforms single forcing by analyzing the spectral power variations of the natural and forced modes. Figures 3 and 5 present the spectral power variations of the natural mode  $(P_n)$ , the forced mode  $(P_f)$ , and the total spectral power of all modes  $(P_t)$  for TO1 and TO2 (denoted by subscripts "1" and "2," respectively), as well as for the entire system (without specific subscript). Spectral power is computed by integrating the power spectral density (PSD)

extracted from the p' signal, using a bandpass filter centered around the relevant frequency with a bandwidth of 0.05 Hz. For total spectral power, the PSD is integrated up to the third super-harmonic of the natural frequency (e.g.,  $3 f_n$ ). All spectral powers of the coupled TOs are normalized by the total spectral power of one TO when unforced but coupled (e.g.,  $(P_{n,1}, P_{f,1}, P_{t,1})/P_{t,c}, P_{t,c}$ =  $P_{t,1}$  =  $P_{t,2}$  when unforced). For decoupled TOs, spectral powers are normalized by the total spectral power of one TO when unfoced and decoupled (e.g.,  $(P_{n,1}, P_{f,1}, P_{t,1})/P_{t,d})$ . The total spectral power of the system is always taken as the sum of contributions from both TOs (e.g.,  $P_t = P_{t,1} + P_{t,2}$ ). To understand how dual forcing and single forcing function differently in suppressing oscillations, two representative forcing frequency ratios  $f_r$  are selected: one above the natural frequency ( $f_r = 1.30$ , Fig. 3) and one below  $(f_r = 0.84, \text{Fig. 5})$ . These cases correspond to the conditions under which the maximum oscillation suppression is achieved on either side of the natural frequency.

As shown in Figs. 3a–f and 5a–f, three distinct regions can be identified based on the variation trends of the spectral power of the natural mode ( $P_n$ ), regardless of the control strategy adopted. The pink region, referred to as "power accumulation", is characterized by unsuppressed  $P_{n,1}$  and  $P_{n,2}$  despite the forcing amplitudes ( $A_1$  and  $A_2$ ) increase. This results in a net accumulation of spectral power, as indicated by rising  $P_{t,1}$  and  $P_{t,2}$ , which reach local maxima. The yellow region, referred to as "power attenuation", is characterized by the suppression of  $P_{n,1}$  and  $P_{n,2}$  as  $A_1$  and  $A_2$  further increase. In this region, the natural modes are strongly weakened, though with different rates at different forcing frequencies, eventually



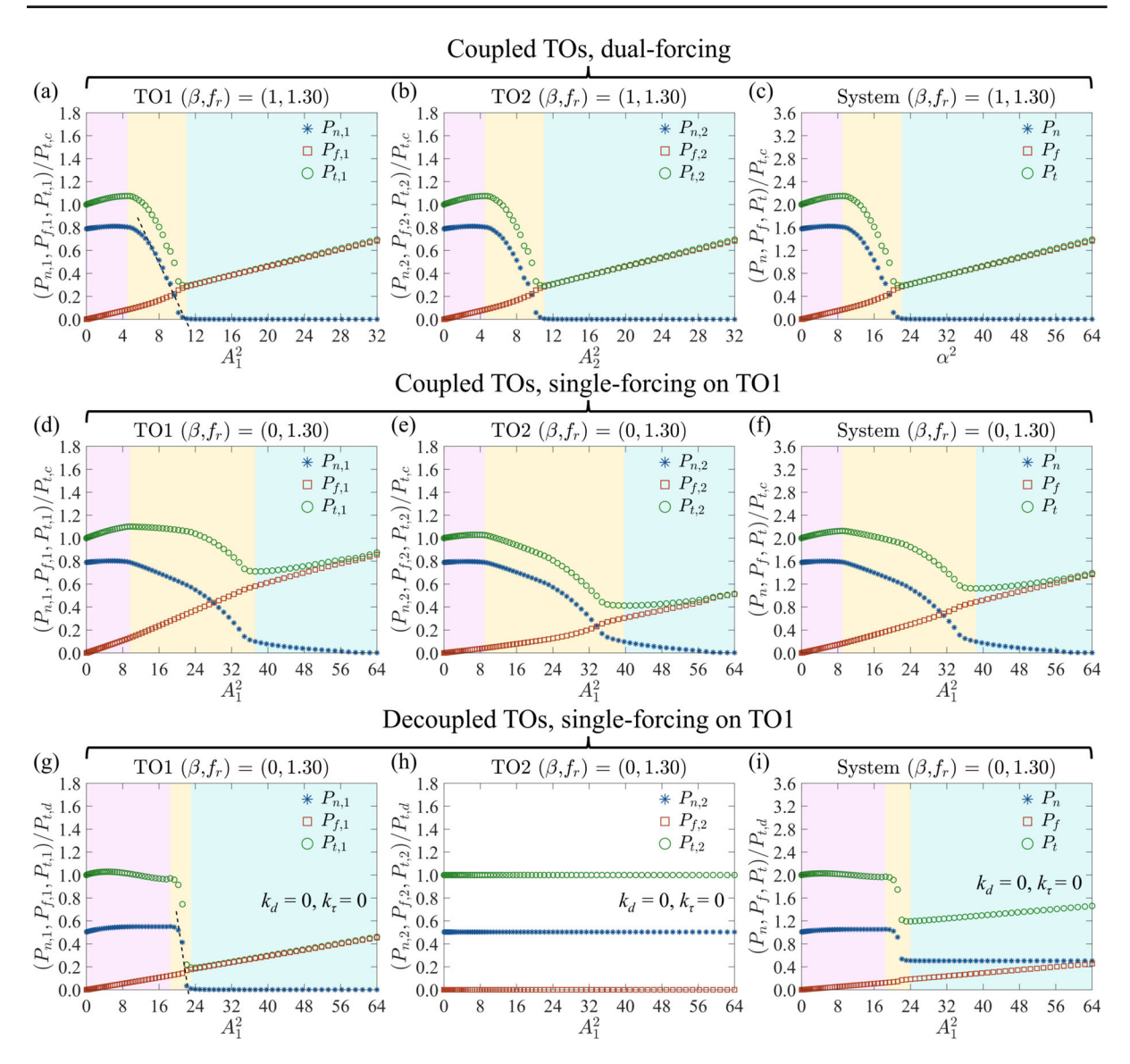


**Fig. 3** Comparison of spectral power variations as a function of squared forcing amplitudes between the coupled TOs under dual forcing (top row), the coupled TOs under single forcing (middle

row), and the decoupled TOs under single forcing (bottom row). The  $f_r$  is fixed to 1.30 for all cases

approaching zero, and maximum oscillation suppression is achieved (i.e., the right boundary of this region is where  $P_{t,1}$  and  $P_{t,2}$  are minimized). Finally, the mint region, referred to as "lock-in", is characterized by domination of the forced mode. Here,  $P_{t,1}$  and  $P_{t,2}$  begin to rise again with increasing  $A_1$  and  $A_2$ , while  $P_{n,1}$  and  $P_{n,2}$  remain essentially constant, indicating that the system has locked into the forcing frequency (i.e. the occurrence of forced synchronization).

We now examine two representative cases ( $f_r = 1.30$  and 0.84) with three different forcing and coupling conditions (coupled TOs under dual forcing, coupled TOs under single forcing, and decoupled TOs under single forcing) in detail as follows:

1. First, we examine the spectral power variation in the "power accumulation" region. For TO1, as  $A_1^2$  increases,  $P_{t,1}$ ,  $P_{n,1}$ , and  $P_{f,1}$  all rise approximately linearly regardless of which forcing strategy



is adopted.  $P_{t,1}$  increases at a noticeably steeper rate than the others, as shown in Fig. 3a, d. This behavior indicates the existence of a "minimum energy threshold": only after the forcing amplitude exceeds a critical value does suppression of the natural oscillation become effective. A similar effect appears in TO1 under single forcing as shown in Fig. 3g, where  $P_{t,1}$  initially increases for small  $A_1^2$ . To the best of our knowledge, this is the first report to explicitly identify a threshold forcing amplitude required for the suppression of natural oscillations—that is, the minimum forcing amplitude necessary for asynchronous quenching to take effect. However, some indirect evidence of this phenomenon can be found in previous studies (e.g., Fig. 9a in [57] and Fig. 8a in [18]), where a temporary increase in  $P_{t,1}$  is observed at very small forcing amplitudes, which potentially explains why this threshold effect has not been emphasized before. For TO2, a similar "power accumulation" region is observed under both forcing strategies, as shown in Fig. 3b, e. In contrast, this feature is absent in the decoupled TO2 case, since the forcing cannot be transmitted to TO2 without coupling, as illustrated in Fig. 3h.

2. Next, we examine the spectral power variation in the "power attenuation" region. For dual forcing shown in Fig. 3a,  $P_{t,1}$  reaches its minimum as  $A_1^2$ increases to a critical value 11.05, corresponding to a 71% reduction in oscillation amplitude compared to the unforced case. Due to the symmetric application of forcing to TO1 and TO2, the same suppression level is observed in both oscillators, as shown in Fig. 3b. When approaching the minimum of  $P_{t,1}$ ,  $P_{n,1}$  decreases nearly linearly with  $A_1^2$ , indicated by the black dashed line in Fig. 3a, with a linear fit yielding an adjusted  $R^2$  value of 0.98. This strongly suggests that the suppression mechanism here is indeed asynchronous quenching and is consistent with previous observations of linear power attenuation behavior [54,55]. This feature is also noticeable for decoupled TO1 under single forcing as shown in Fig. 3g that  $P_{n,1}$  drops rapidly as  $A_1^2$  increases. However, it is also worth noting that the slope of this power attenuation of the decoupled TO1 under single forcing is steeper than that of the coupled TO1 under dual forcing (-0.269 < -0.169, indicated by the two dashed lines in Fig. 3a and g). This indicates that the efficiency of power attenuation purely caused by forcing is likely to be deterio-

rated by the existence of the coupling. This is more noticeable for the coupled TOs under single forcing. This asymmetric application of forcing to TO1 further requires the forcing energy to be transferred from TO1 (the one being directly forced) to TO2 (the other one being indirectly forced). The power attenuation slope of the natural mode is flatter, and the variation becomes clearly nonlinear, as indicated by the behavior of  $P_{n,1}$  and  $P_{n,2}$  in Fig. 3d, e. These observations suggest that coupling acts as an additional damping source, which partially offsets the attenuation induced by forcing. This nonlinear mode transition induced by external forcing exhibits characteristic similarities to the Bogdanov-Takens resonance described by Coccolo et al. [27]. Their study reveals a coupling mechanism between the system's sensitivity along the bifurcation path and nonlinear dissipation. Such a resonance typically occurs when the system operates near a bifurcation boundary, exhibiting high sensitivity to weak external forcing, which can trigger transitions between coexisting attractors. To further examine this hypothesis, we calculate the power dissipated through both dissipative and time-delay coupling for TO1 and TO2 under dual forcing and single forcing. Based on the formulations given in Eqs. 14 and 16, we perform the following integrations:

$$P_{d,1} = \int k_d (\dot{\eta}_{2,j} - \dot{\eta}_{1,j}) \dot{\eta}_{1,j} dt,$$

$$P_{d,2} = \int k_d (\dot{\eta}_{1,j} - \dot{\eta}_{2,j}) \dot{\eta}_{2,j} dt,$$

$$P_d = P_{d,1} + P_{d,2} = -\int k_d (\dot{\eta}_{1,j} - \dot{\eta}_{2,j})^2 dt.$$
(17)

$$P_{\tau,1} = \int k_{\tau} \left[ \dot{\eta}_{2,j}(t - \tau_{tube}) \dot{\eta}_{1,j} - \dot{\eta}_{1,j}^{2}(t) \right] dt,$$

$$P_{\tau,2} = \int k_{\tau} \left[ \dot{\eta}_{1,j}(t - \tau_{tube}) \dot{\eta}_{2,j} - \dot{\eta}_{2,j}^{2}(t) \right] dt,$$

$$P_{\tau} = P_{\tau,1} + P_{\tau,2}.$$
(18)

As shown in Fig. 4a, b, under dual forcing, the power dissipated via dissipative coupling remains zero across all forcing amplitudes. In contrast, the power dissipated by time-delay coupling initially remains nearly constant at a large negative value and then increases significantly, peaking around  $\alpha \approx$ 



22—coinciding with the point of maximum amplitude reduction. This trend aligns with the spectral power behavior discussed earlier: (1) in the "power accumulation" region, all spectral components intensify while energy dissipation is negligible, likely because  $P_{\tau}$  remains nearly unchanged up to  $\alpha^2 \approx 9$ ; and (2) in the "power attenuation" region,  $P_{\tau}$  rises sharply (i.e., becomes less negative), indicating that less spectral power of the natural mode is being dissipated via time-delay coupling, as most of it is now being attenuated by forcing. Under single forcing, the impact of coupling becomes more pronounced. In this case, the dissipative coupling begins to significantly damp the forcing energy. As shown in Fig. 4d, e, the dissipative power increases notably with forcing amplitude, and  $P_{d,2}$  is much smaller than  $P_{d,1}$ —likely because the forcing is applied solely to TO1. The variations in  $P_{\tau,1}$  and  $P_{\tau,2}$  differ from one another and also deviate from those observed under dual forcing scenario, which can be attributed to the asymmetric application of forcing to TO1 only, where energy is injected into TO1 and subsequently transferred to TO2. Notably, the total power dissipation via coupling  $(P_d + P_{\tau})$ under single forcing (Fig. 4f) is much larger in magnitude (i.e., more negative) than under dual forcing (Fig. 4c). This elevated dissipation is likely a key factor explaining why dual forcing is more effective than single forcing in suppressing oscillations.

3. Last, we examine the spectral power variation in the "lock-in" region. As shown in Fig. 3a, b and Fig. 3d, e,  $P_{n,1}$  and  $P_{n,2}$  are significantly small values and asymptotically approach 0 as the forcing amplitude increases, indicating the significant suppression of the natural mode. As shown in Figs. 3a, b, d, e, the gap of the spectral power between  $P_{f,1}$  and  $P_{t,1}$ , and  $P_{f,2}$  and  $P_{t,2}$  are shrinking further to a negligible magnitude, indicating the dominance of the forced mode in the system.

All the aforementioned observations are also found at  $f_r = 0.84$  as shown in Figs. 5 and 6, confirming that the core mechanism behind the superior performance of dual forcing lies in the reduced dissipation induced by coupling as the forcing amplitude increases. In contrast, under single forcing, the energy injected by forcing is less efficiently utilized to suppress the natural mode, as a portion of it is dissipated through the coupling between the two TOs—undesirably off-

setting the intended suppression effect. It should be noted that while this study reveals the trends of energy dissipation through power spectral density analysis, the current understanding of the underlying energy transfer mechanisms is primarily derived from numerical simulations. To gain a more comprehensive and fundamental insight into this phenomenon, future work could incorporate analytical approaches, such as perturbation methods.

### 3.4 Phase modulation of two forcing inputs $\phi$

The spectral power analysis presented in Sect. 3.3 reveals that the maximum oscillation suppression is primarily constrained by the amount of energy accumulated in the forced mode  $(P_f)$ , particularly when the spectral power of the natural mode  $(P_n)$  is significantly diminished, or even completely suppressed sometimes, by the external forcing. Once the forcing amplitude exceeds the critical value that yields this maximum reduction, further increases in forcing amplitude lead to a deteriorating reduction effect. This occurs because the natural mode no longer contributes to the spectral power reduction, while the spectral power associated with the forced mode continues to rise, resulting in an overall increase in total spectral power. This trend has also been observed in experimental studies of both laminar [39,40] and turbulent [37,41] thermoacoustic systems subjected to the external forcing. Leveraging the additional flexibility offered by using dual forcing, the following two sections investigate whether tuning the phase between the two forcing inputs can reduce spectral power accumulation in the forced mode, and whether frequency detuning between the two forcing inputs can further enhance oscillation suppression.

In this section, we continue analyzing two representative cases ( $f_r=0.84$  and  $f_r=1.30$ ) under the critical forcing conditions that yield maximum oscillation suppression—specifically,  $\beta=1$  with  $\alpha=4.1$  for  $f_r=0.84$  and  $\alpha=4.7$  for  $f_r=1.30$ . We systematically vary  $\phi$ , defined as the initial phase difference between the two forcing signals—namely,  $A_1\sin(2\pi f_{f,1}t)$  and  $A_2\sin(2\pi f_{f,2}t+\phi)$ —from  $0^\circ$  to  $360^\circ$ . Figures 7 and 8 show the influence of  $\phi$  on the suppression performance of the system. The value of  $\mathcal E$  at each  $\phi$  is normalized by  $\mathcal E$  at  $\phi=0^\circ$  (i.e., no phase modulation case). A normalized value  $\mathcal E_\phi/\mathcal E_{\phi=0^\circ}$  greater than 1 (shaded in light gray) indicates improved



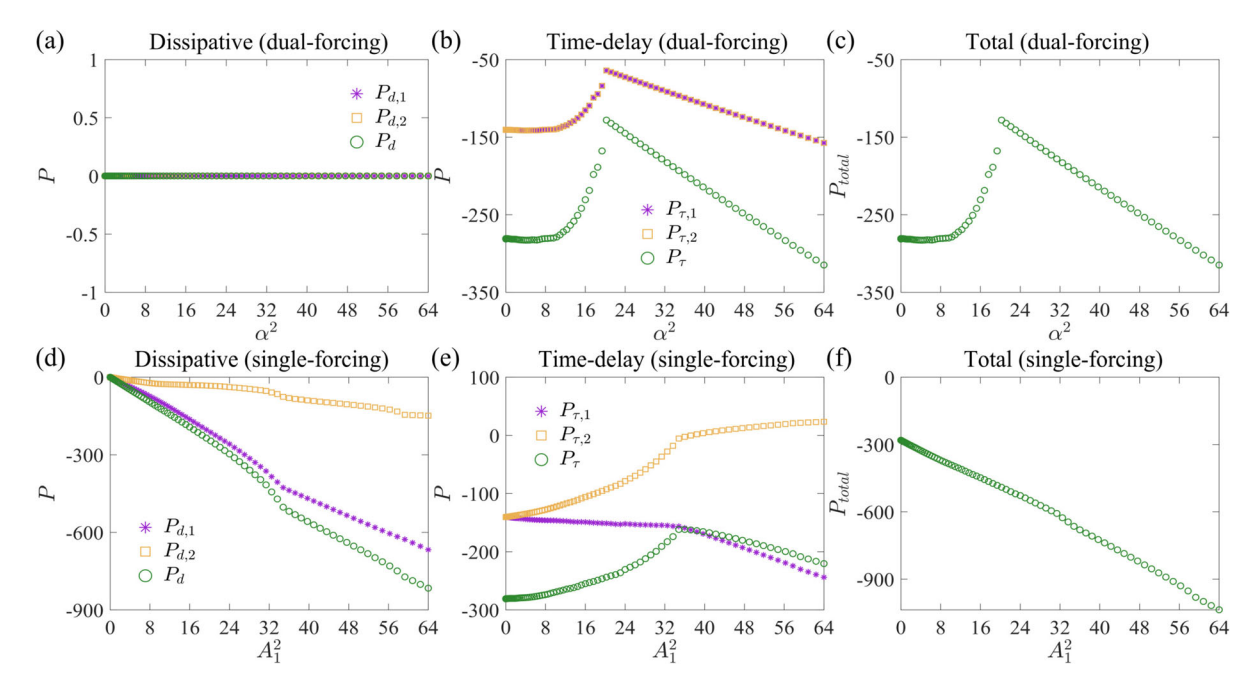


**Fig. 4** Comparisons of energy dissipations by a dissipative coupling, b time-delay coupling, and c the total of two coupling methods, as a function of squared forcing amplitudes between

the coupled TOs under dual forcing (top row) and single forcing (bottom row). The  $f_r$  is fixed to 1.30 for all cases

suppression due to phase modulation, whereas a value less than 1 suggests a deterioration in suppression. Notably, a negative normalized value implies that phase modulation even amplifies the oscillations rather than suppressing them.

As shown in Fig. 7a, when  $\phi$  increases from  $0^{\circ}$ to 35°, suppression result deteriorates for TO1 but improves for TO2. Since the relative improvement in TO2 outweighs the deterioration in TO1, Fig. 7b shows an overall enhanced suppression result, with optimal suppression occurring at  $\phi = 35^{\circ}$ , where  $\mathcal{E}_{\phi} = -0.48$ , corresponding to a 2% improvement relative to the baseline case at  $\phi = 0^{\circ}$ . Similarly, Fig. 8a shows that for the case  $(\alpha, \beta, f_r) = (4.1, 1, 0.84)$ , the suppression result at  $\phi = 0^{\circ}$  is  $\mathcal{E}_{\phi=0^{\circ}} = -0.43$ . As  $\phi$  increases to 23°, TO1 exhibits improved suppression while TO2 shows deterioration; however, the net effect is positive, with TO1's improvement dominating. A similar trend is observed as  $\phi$  further increases. According to Fig. 8b, the optimal suppression occurs at  $\phi = 337^{\circ}$ , with  $\mathcal{E}_{\phi} = -0.45$ , marking an improvement of up to 5% (at  $\phi = 23^{\circ}$ ) compared to the baseline case at  $\phi = 0^{\circ}$ .

Initially, we hypothesized that setting the phase difference between the two forcing inputs to 180° might lead to their mutual cancellation, thereby enhancing suppression by annihilating the remaining energy of the forced mode. However, our results show that this specific approach ( $\phi = 180^{\circ}$ ) does not yield improved suppression performance in practice. We speculate that this is because the spectral power of the forced mode reflects the system's response at the forcing frequency, rather than the residual energy of the input forcing itself. Although phase modulation can achieve an additional  $\approx$ 5% reduction in oscillation amplitude under optimal conditions (as shown in Figs. 7 and 8), the system is already operating near the suppression limit in this regime, where most of the suppression potential has been exploited through open-loop forcing. Therefore, phase modulation is better suited as a complementary strategy for fine-tuning parameters rather than serving as a primary control mechanism. Furthermore, we acknowledge that the promising numerical results require experimental validation to confirm their practical feasibility. As a result, phase modulation between the two forcing inputs does not lead to complete cancellation of the forced response in the system and, consequently, does not produce a significant improvement in suppression.



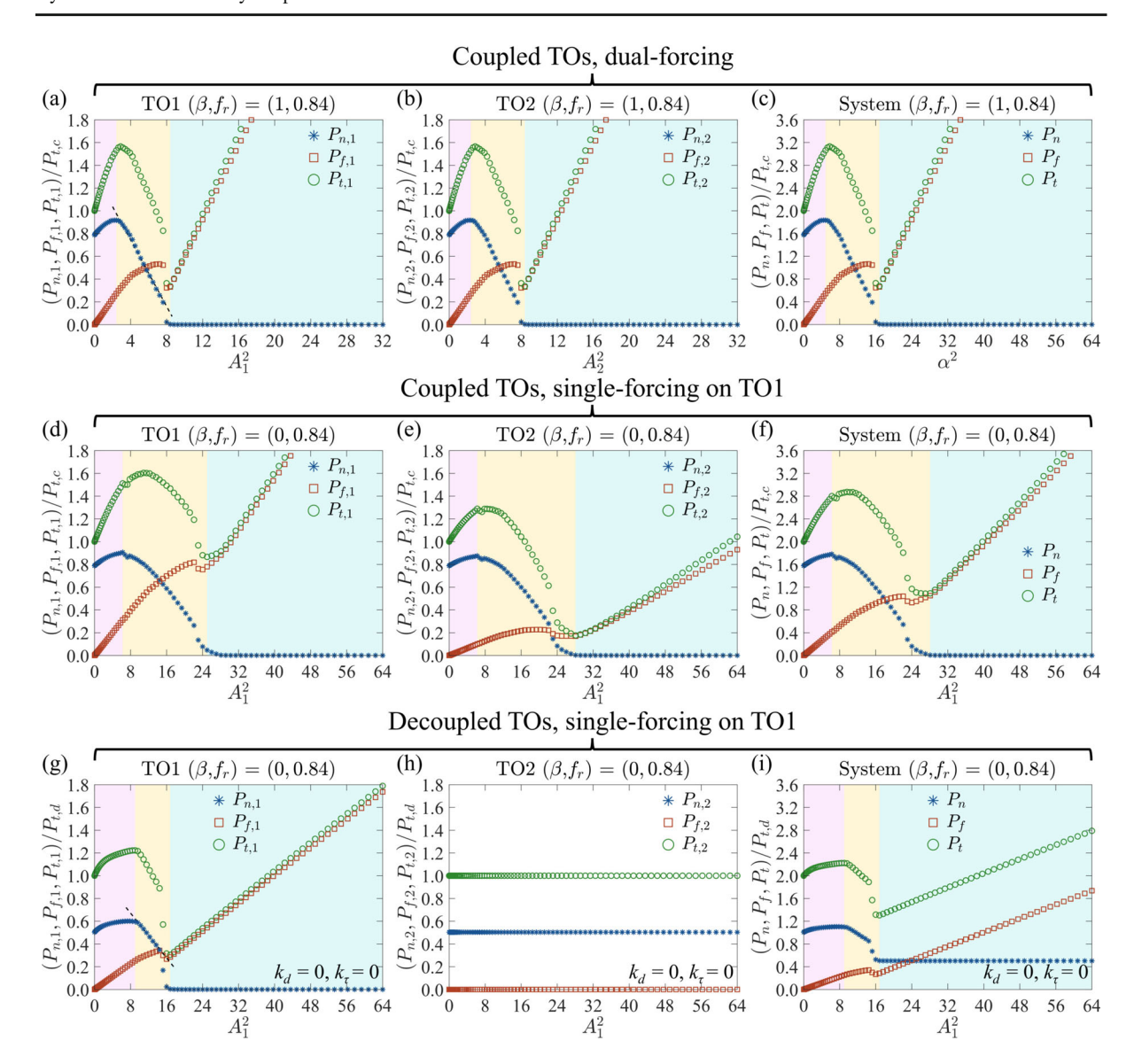


**Fig. 5** The same as for Fig. 3 but for  $f_r = 0.84$ 

# 3.5 Frequency detuning between two forcing inputs $f_{r,1} \neq f_{r,2}$

In Sect. 3.4, we demonstrated that the additional flexibility offered by introducing secondary forcing can be leveraged to adjust the phase between the two forcing inputs, thereby enhancing oscillation suppression. In this section, we further investigate whether detuning the secondary forcing frequency can achieve a similar enhancement. We focus again on the two representative cases that yielded the most effective suppression across

our entire parameter space. Instead of using two identical forcing frequencies, we now introduce two distinct ones:  $f_{r,1} = f_{f,1}/f_n$  and  $f_{r,2} = f_{f,2}/f_n$ . We fix  $f_{r,1}$  at 1.30 or 0.84 and vary  $f_{r,2}$  within the range 0.70–1.30 in steps of 0.01. Figures 9 show how the system's response changes as  $f_{r,2}$  varies. The suppression performance at each detuned  $f_{r,2}$  is normalized by the baseline cases with  $f_{r,1} = f_{r,2} = 1.30$  (Fig. 9a) and  $f_{r,1} = f_{r,2} = 0.84$  (Fig. 9b), respectively. Similar to Fig. 8, a normalized amplitude ratio  $\mathcal{E}_f/\mathcal{E}_{f,1}=f_{f,2}>1$  indicates improved suppression compared to the identical-



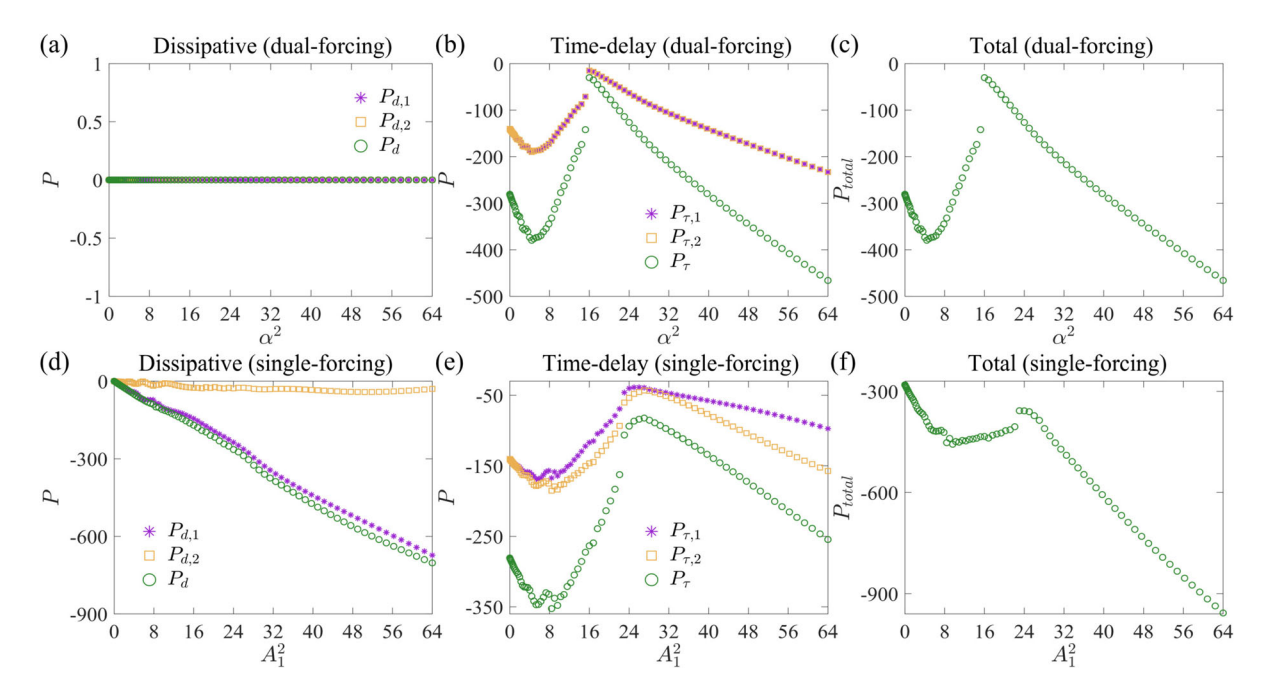


**Fig. 6** The same as for Fig. 4 but for  $f_r = 0.84$ 

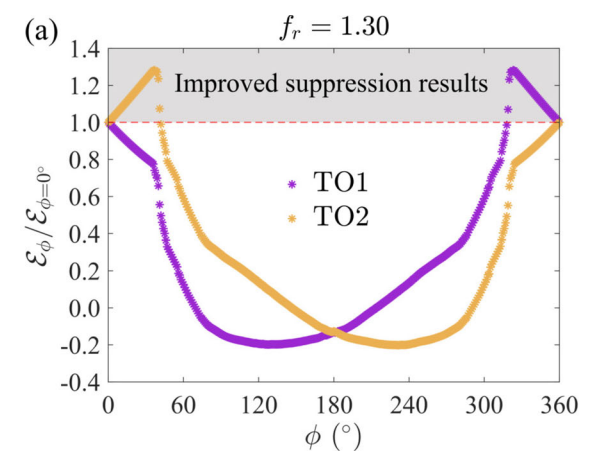
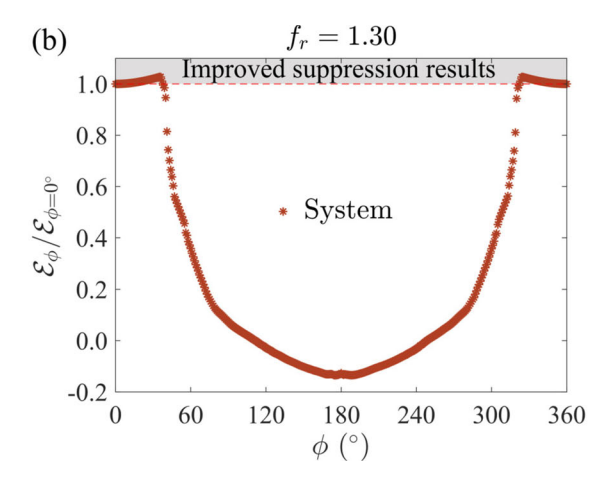


**Fig. 7** Variations of  $\mathcal E$  normalized by  $\mathcal E_{\phi=0^\circ}$  (i.e., the case without phase modulation), as a function of the modulated phase angle  $\phi$  for  $\mathbf a$  two TOs and  $\mathbf b$  the overall system. Phase modulation yields

frequency case, while  $0 < \mathcal{E}_f/\mathcal{E}_{f_{f,1}=f_{f,2}} < 1$  suggests reduced but still effective suppression. A ratio  $\mathcal{E}_f/\mathcal{E}_{f_{f,1}=f_{f,2}} < 0$  indicates amplitude amplification. The results clearly show that frequency detuning does not lead to improved suppression: no case with  $f_{r,1} \neq f_{r,2}$  outperforms the identical-frequency configuration. Notably, even the combination of the two best individual frequencies (1.30 and 0.84) results in diminished performance. This suggests that there is no synergistic



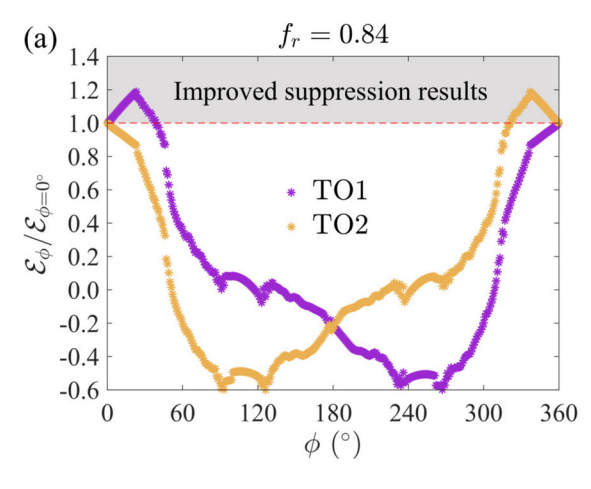
enhanced oscillation suppression in the region beyond the red dashed line. The  $f_r$  is fixed to 1.30 for all cases

effect from using two different forcing frequencies, and that identical dual forcing remains the optimal configuration.

## 4 Conclusions

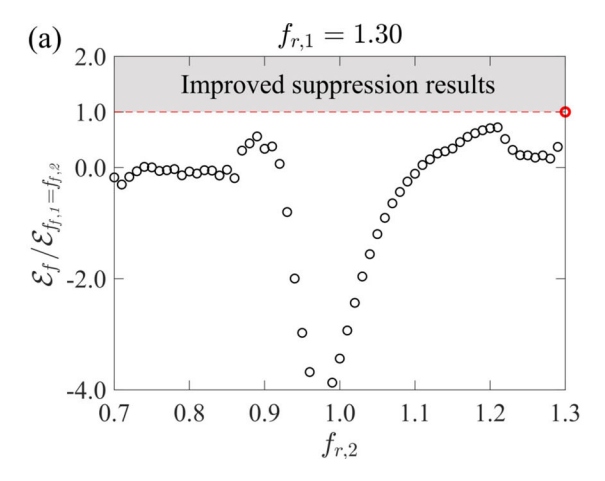
In this study, the dynamics of two coupled thermoacoustic oscillators (TOs) under external dual forcing are





 $f_r = 0.84$ (b) Improved suppression results 1.0 0.8 0.6 System 0.4 0.2 0.0 -0.2-0.40 60 120 180 240 300 360  $\phi$  (°)

**Fig. 8** The same as for Fig. 7 but for  $f_r = 0.84$ 



(b)  $f_{r,1} = 0.84$ Improved suppression results  $f_{r,0} = 0.0$   $f_{r,1} = 0.84$ Improved suppression results  $f_{r,0} = 0.0$   $f_{r,0} = 0.0$ 

**Fig. 9** Variations of  $\mathcal{E}$ , normalized by  $\mathcal{E}_{f_{f,1}=f_{f,2}}$  (i.e., the case without frequency detuning), as a function of the detuned forcing frequency  $f_{f,2}$  for the overall system. Enhanced oscillation

suppression (if any) is observed in the gray region beyond the red dashed line. The reference forcing frequency  $f_{f,1}$  is fixed at a 1.30 and **b** 0.84 in all cases

numerically investigated. The system's forced response is systematically explored in a parameter space defined by three key parameters: the forcing amplitude ratio  $(\beta)$ , the total forcing amplitude  $(\alpha)$ , and the forcing frequency  $(f_r)$ . The answers to the three research questions posed in Sect. 3.1 are summarized as follows:

- 1. Dual forcing is shown to outperform single forcing when the forcing energy is approximately equally distributed between the two forcing inputs, resulting in up to 60% greater amplitude reduction.
- 2. The optimal forcing condition occurs when the forcing frequency  $f_r$  deviates sufficiently away from the system's natural frequency,  $\beta = 1$ , and  $\alpha$  is sufficiently large to trigger asynchronous quenching. At  $f_r = 1.30$ , the most significant suppression

of oscillations is achieved, with amplitude reductions reaching  $\mathcal{E} = -0.43$ . This corresponds to a 57% reduction in the RMS amplitude of pressure oscillations relative to the unforced case. Furthermore, this suppression can be enhanced by phase modulation between the two forcing inputs, yielding an additional 5% reduction. However, introducing frequency detuning between the two forcing inputs does not improve suppression. Additionally, the system's response is sensitive to the  $f_r$ , but the optimal values for  $\alpha$ ,  $\beta$ , and  $\phi$  exist within certain ranges.

 Spectral power analysis reveals the underlying mechanism behind the superior performance of dual forcing. Unlike single forcing, dual forcing minimizes the energy dissipation through coupling.



When adopting single forcing, a significant portion of the forcing energy is likely lost during its transfer between TOs via coupling, reducing its efficiency in suppressing the natural mode. Therefore, for a fixed amount of forcing energy, dual forcing achieves more effective and efficient suppression of thermoacoustic oscillations.

In summary, these findings highlight the strong potential of employing a symmetric forcing strategy to suppress oscillations in systems comprising multiple mutually coupled thermoacoustic oscillators [58,59] particularly when modifying the coupling condition to passively stabilize the system is challenging. While introducing symmetry breaking has been shown in recent numerical and experimental studies [26,60,61] to enhance thermoacoustic stability in some multiinjector/combustor systems, this principle does not hold here when the external forcing is deployed to suppress oscillations. In such cases, coupling tends to dissipate energy during the transfer of forcing between oscillators, thereby reducing the effectiveness when adopting asymmetric forcing configurations. Finally, we realize the limitations of the current numerical approach; a follow-up experimental study, guided by these numerical results, is planned for future work.

Author contributions Chenjun Zhao: data curation, formal analysis, software, visualization, validation, writing—original draft; Liheng Zheng: writing—review & editing; Jie Zhou: funding acquisition, writing—review & editing; Yu Guan: conceptualization, methodology, funding acquisition, writing—original draft, writing—review & editing

Fig. 10 Characteristic of a single uncoupled TO, pressure amplitude  $\mathcal{E}$  as a function of the nondimensional heater power K

**Funding** Open access funding provided by The Hong Kong Polytechnic University This work was supported by the National Natural Science Foundation of China (Grant No. 52306166) and the Hong Kong Innovation and Technology Commission (Grant No. GHP/100/22GD). JZ was supported by the National Natural Science Foundation of China (Grant No. 12472092).

**Data Availability Statement** The data that support the findings of this study are available upon reasonable request.

#### **Declarations**

**Conflict of interest** The authors declare that they have no conflict of interest.

**Open Access** This article is licensed under a Creative Commons Attribution 4.0 International License, which permits use, sharing, adaptation, distribution and reproduction in any medium or format, as long as you give appropriate credit to the original author(s) and the source, provide a link to the Creative Commons licence, and indicate if changes were made. The images or other third party material in this article are included in the article's Creative Commons licence, unless indicated otherwise in a credit line to the material. If material is not included in the article's Creative Commons licence and your intended use is not permitted by statutory regulation or exceeds the permitted use, you will need to obtain permission directly from the copyright holder. To view a copy of this licence, visit http://creativecommons.org/licenses/by/4.0/.

### Appendix A Validation of our numerical scheme

We test the convergence of Galerkin truncation by validating the bifurcation behavior of a single uncoupled TO with different modes. We numerically solve



the ODEs in Eqs. (10-12). According to Fig. 10, we can clearly see that the difference between the bifurcation diagram at N = 4 (red line with square markers) and N = 5 (green star markers) is significant. However, there is almost no difference between N = 5 (green star markers) and N = 10 (blue line with circles). Therefore, in order to balance accuracy and computational efficiency, we chose N = 5.

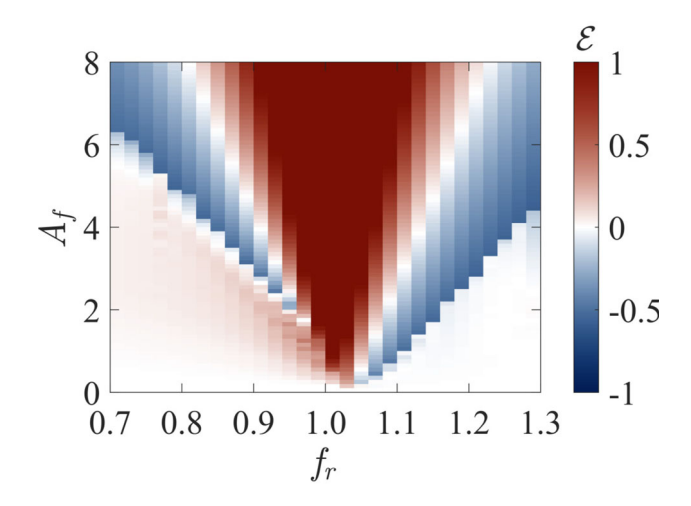
We validate our numerical scheme by examining the forced response of a single TO under single forcing. Specifically, a forcing term of the form  $A_f \sin(2\pi f_f t)$ 

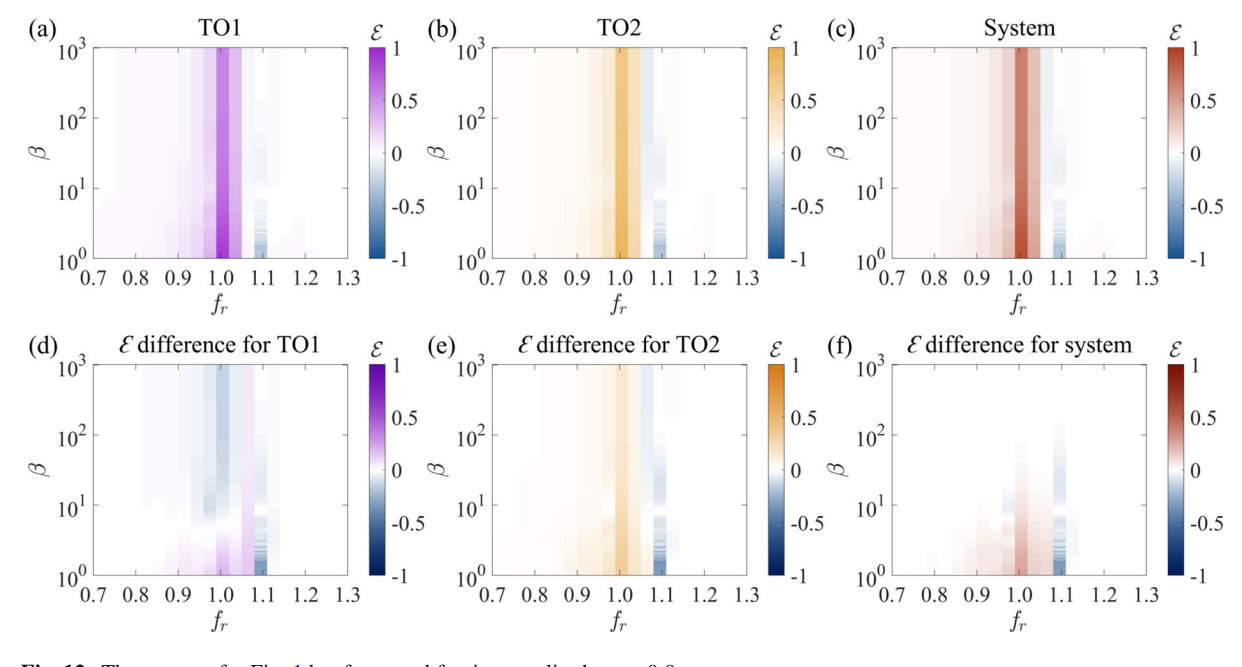
is added to the right-hand side of Eq. 10, with the heating power kept the same as in Sect. 2 (K = 2), and the normalized forcing frequency defined as  $f_r = f_f/f_n$ . We numerically solve Eqs. 10–12 using dde23, a builtin delay differential equation solver in MATLAB® [62]. In Fig. 11, the  $A_f - f_f$  two-parameter map reveals regions of asynchronous quenching (blue) and resonance amplification (red), consistent with previous experimental observations reported in the literature [17].

System

Fig. 11 The forced response of a single TO under single forcing

TO1





TO2

**Fig. 12** The same as for Fig. 1 but for a total forcing amplitude  $\alpha = 0.9$ 

 $\mathcal{E}$ 

### Appendix B Supplementary cases for $\beta$

The regions where dual forcing outperforms single forcing vary with  $\alpha$ , as shown in Figs. 12, 13, 14, and 15. Notably, the size of these regions—where dual forcing demonstrates superior control—expands significantly as  $\alpha$  increases. This trend supports our earlier observation that dual forcing becomes increasingly effective at suppressing oscillations with a greater forcing amplitude, making it a better approach overall.

# Appendix C Sensitivity analysis of small mismatches in K, $\tau$ , $\zeta$

The influence of parametric noise in thermoacoustic systems has been investigated in prior studies, e.g., by Daw et al. [63], Bonciolini et al. [64], and Burnley and Culick [65]. Drawing inspiration from these previous works, we introduce noise into three parameters in our model, including K,  $\tau$ , and  $\zeta$ . The corresponding parameters with the noise term can be expressed as follows:

$$X_n = X_0 [1 + \sigma_p \varepsilon(t)],$$
  

$$(X = K/\tau/\zeta),$$
(C1)

where  $X_n$  and  $X_0$  represent the parameters with and without a small mismatch, respectively. To determine the strength of parametric mismatch, we refer to [63– 65], where the strength is typically specified to be less than 1%. Therefore, we set  $\sigma_p = 0.01$ . We generated 10 sets of random samples, with error bars added to the results to assess the stability of the model under perturbations. Specifically, two cases discussed in the paper were analyzed, corresponding to  $\alpha = 4.1$  and 4.7 with  $\beta = 1$ . We introduced mismatches to the parameters K,  $\tau$ , and  $\zeta$  for TO1 and TO2, resulting in  $K_1$ ,  $K_2$ ,  $\tau_1$ ,  $\tau_2$ ,  $\zeta_1$ , and  $\zeta_2$ . As shown in Fig. 16a–f, the horizontal axis represents  $f_r$ , and the vertical axis represents  $\mathcal{E}$ . The blue curve denotes data without parameter mismatches, while the red curve represents the average of the 10 mismatched datasets. Error bars indicate the fluctuation range at each data point. It can be observed that the variation at each data point remains extremely small, with a maximum deviation not exceeding 0.01. Thus, the analysis suggests that the system is relatively

insensitive to small mismatches in K,  $\tau$ , and  $\zeta$ , confirming that the model is robust even with small variations in the parameters.

# Appendix D Impact of additive noise on suppression performance

In our study, we introduced additive noise to explore its impact on the suppression outcome of the system. We used Gaussian white noise and performed detailed calculations and analyses on the system's behavior. The results indicate that, even with the introduction of noise, the suppression effect of the system is not significantly affected. We analyzed two cases discussed in Sect. 3.3, namely  $\alpha=4.7$  (Fig. 17a) and  $\alpha=4.1$  (Fig. 17a), with  $\beta=1$ . Our Rijke tube model (Eqs. C2) becomes Eqs. (C2) after introducing the noise source term, as follows:

$$\frac{\mathrm{d}\dot{\eta}_{1,j}}{\mathrm{d}t} + 2\xi_{j}\omega_{j}\dot{\eta}_{1,j} + \omega_{j}^{2}\eta_{1,j}$$

$$= -j\pi K \left[ \sqrt{\left| \frac{1}{3} + u'_{f,1}(t - \tau_{t}) \right|} - \sqrt{\frac{1}{3}} \right] \sin\left(j\pi x_{f}\right)$$

$$+ \underbrace{k_{d}\left(\dot{\eta}_{2,j} - \dot{\eta}_{1,j}\right)}_{\mathrm{dissipative coupling}} + \underbrace{k_{\tau}\left(\dot{\eta}_{2,j}(t - \tau_{\text{tube}}) - \dot{\eta}_{1,j}(t)\right)}_{\mathrm{forcing term}} + \underbrace{\sigma\varepsilon(t)}_{\mathrm{noise}}, \tag{C2}$$

where  $\sigma$  is the noise intensity,  $\varepsilon(t)$  is the Gaussian white noise term, and all other parameters are identical to those in Eq. 14. We chose  $\sigma=0.05$  as the noise intensity. We used the Monte Carlo method to randomly generate 100 sets of random samples. By calculating the mean and standard deviation of the 100 random perturbations, we obtained the system's response. The error bars indicate the range of fluctuation, with the maximum error not exceeding 0.016, suggesting that the additive noise has a negligible effect on the suppression performance of the thermoacoustic oscillators.



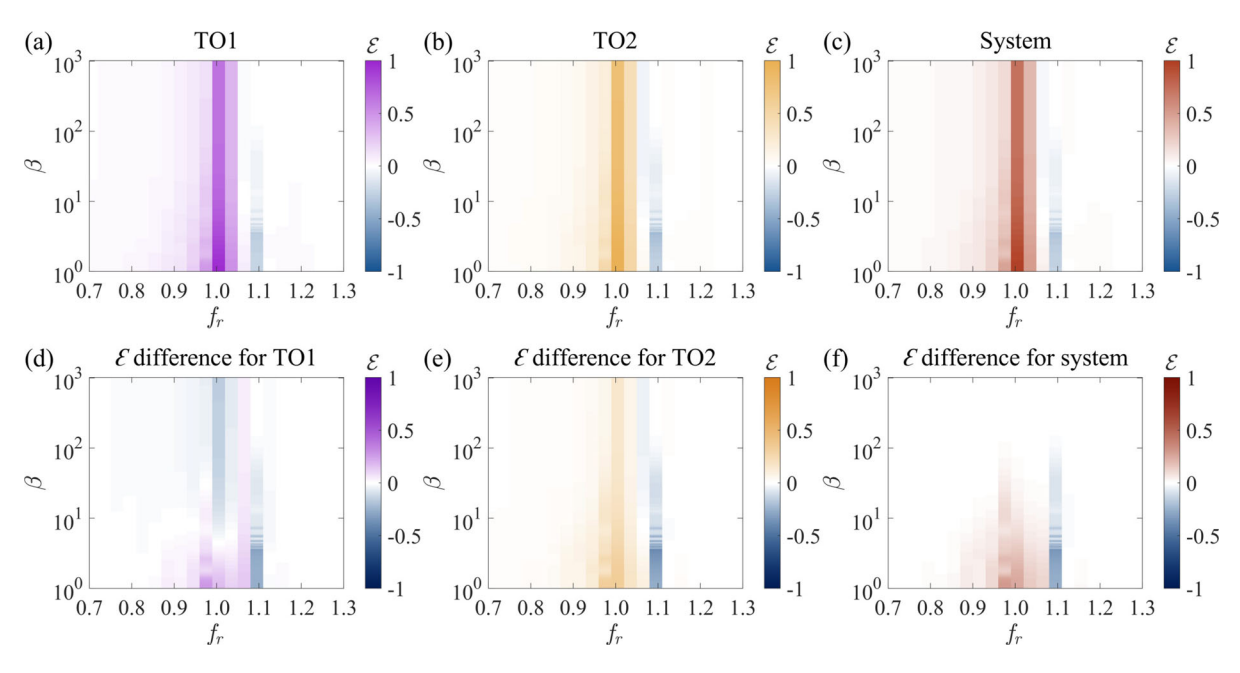


**Fig. 13** The same as for Fig. 1, but for a total forcing amplitude  $\alpha = 1$ 

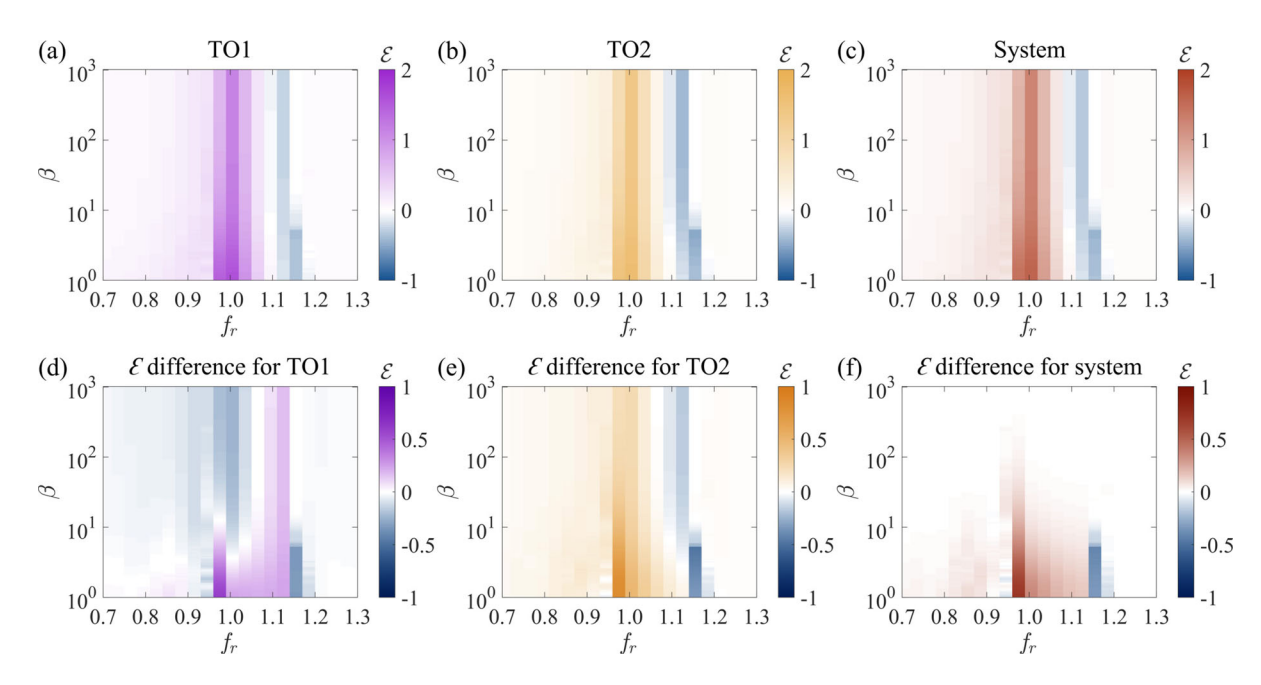


**Fig. 14** The same as for Fig. 1 but for a total forcing amplitude  $\alpha = 2$ 

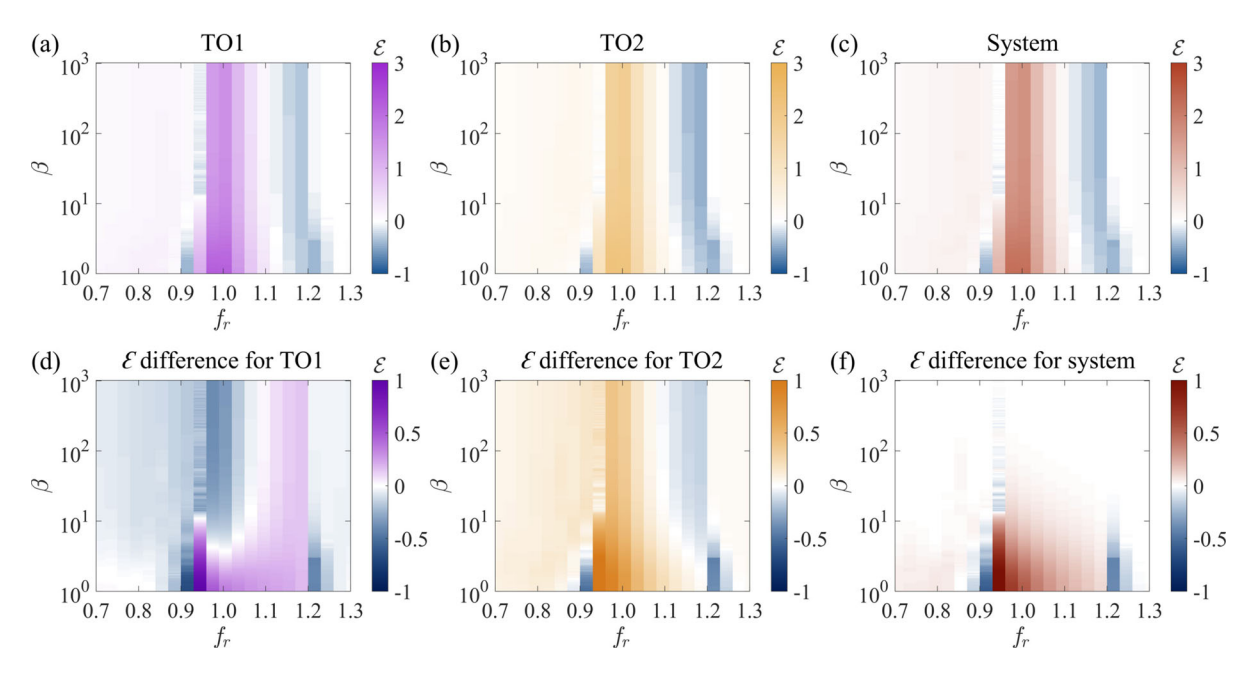


**Fig. 15** The same as for Fig. 1 but for a total forcing amplitude  $\alpha = 3$ 

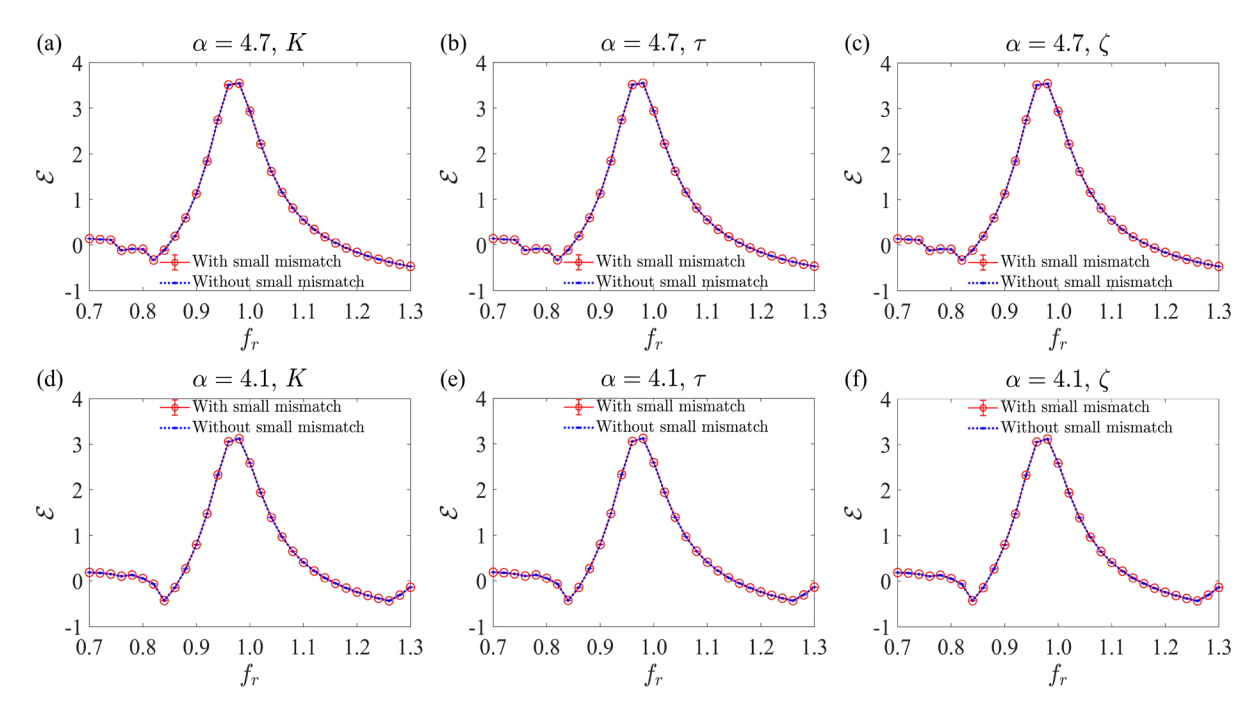


**Fig. 16** Comparison of system dynamics with and without a small mismatch for different parameter perturbations. **a**  $\alpha = 4.7$ , K; **b**  $\alpha = 4.7$ ,  $\tau$ ; **c**  $\alpha = 4.7$ ,  $\zeta$ ; **d**  $\alpha = 4.1$ , K; **e**  $\alpha = 4.1$ ,  $\tau$ ; **f**  $\alpha = 4.1$ ,  $\zeta$ . The horizontal axis represents the frequency ratio  $f_r$ , and the vertical axis represents the system response  $\mathcal{E}$ . The

blue circles correspond to the case without a small mismatch, while the red squares represent the case with a small mismatch. The error bars represent the mean and standard deviation of the system response across 10 sets of random perturbations. (Color figure online)



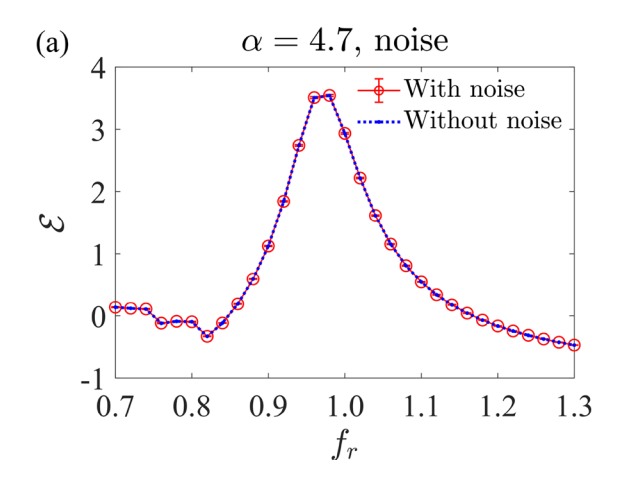
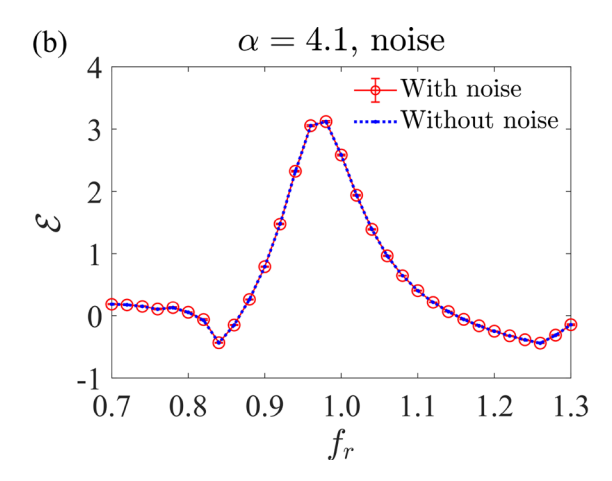


**Fig. 17** Comparison of system behavior with and without additive noise. **a**  $\alpha = 4.7$  (Fig. 17a); **b**  $\alpha = 4.1$  (Fig. 17b). The horizontal axis represents the frequency ratio  $f_r$ , and the vertical axis represents the system response  $\mathcal{E}$ . The blue circles corre-



spond to the system behavior without noise, while the red squares represent the system behavior with additive noise. The error bars represent the mean and standard deviation of the system response across 100 sets of random perturbations. (Color figure online)

#### References

- Lieuwen, T., Yang, V.: Combustion Instabilities in Gas Turbine Engines: Operational Experience, Fundamental Mechanisms, and Modeling. American Institute of Aeronautics and Astronautics, Reston (2005)
- Huang, Y., Yang, V.: Dynamics and stability of leanpremixed swirl-stabilized combustion. Prog. Energy Combust. Sci. 35(4), 293–364 (2009)
- O'Connor, J.: Understanding the role of flow dynamics in thermoacoustic combustion instability. Proc. Combust. Inst. 39(4), 4583–4610 (2023)
- Morgans, A., Yang, D.: Thermoacoustic instability in combustors. Annu. Rev. Fluid Mech. 57, 9–33 (2024)
- Ghirardo, G., Di Giovine, C., Moeck, J., Bothien, M.: Thermoacoustics of can-annular combustors. J. Eng. Gas Turbines Power 141(1), 011007 (2019)
- Guan, Y., Moon, K., Kim, K., Li, L.: Synchronization and chimeras in a network of four ring-coupled thermoacoustic oscillators. J. Fluid Mech. 938, 5 (2022)
- Orchini, A., Moeck, J.: Weakly nonlinear analysis of thermoacoustic oscillations in can-annular combustors. J. Fluid Mech. 980, 52 (2024)
- 8. Sujith, R., Pawar, S.: Thermoacoustic Instability. Springer, Germany (2021)
- Juniper, M.: Sensitivity and nonlinearity of thermoacoustic oscillations. Annu. Rev. Fluid Mech. 50(1), 661–689 (2018)
- Jegal, H., Moon, K., Gu, J., Li, L., Kim, K.: Mutual synchronization of two lean-premixed gas turbine combustors: phase locking and amplitude death. Combust. Flame 206, 424–437 (2019)
- Ghosh, A., Sujith, R.: Emergence of order from chaos: a phenomenological model of coupled oscillators. Chaos, Solitons & Fractals 141, 110334 (2020)

- 12. Ghosh, A., Pawar, S., Sujith, R.: Anticipating synchrony in dynamical systems using information theory. Chaos **32**(3), 031103 (2022)
- Guan, Y., Moon, K., Kim, K., Li, L.: Low-order modeling of the mutual synchronization between two turbulent thermoacoustic oscillators. Phys. Rev. E 104(2), 024216 (2021)
- Liao, Y., Guan, Y., Liu, P., Moon, K., Kim, K.: Low-order modeling of collective dynamics of four ring-coupled turbulent thermoacoustic oscillators. Nonlinear Dyn. 112(9), 6897–6917 (2024)
- Moon, K., Guan, Y., Li, L., Kim, K.: Mutual synchronization of two flame-driven thermoacoustic oscillators: dissipative and time-delayed coupling effects. Chaos 30(2), 023110 (2020)
- Moon, K., Yoon, C., Kim, K.: Influence of rotational asymmetry on thermoacoustic instabilities in a can-annular lean-premixed combustor. Combust. Flame 223, 295–306 (2021)
- Sahay, A., Roy, A., Pawar, S., Sujith, R.: Dynamics of coupled thermoacoustic oscillators under asymmetric forcing. Phys. Rev. Appl. 15(4), 044011 (2021)
- Mondal, S., Pawar, S., Sujith, R.: Forced synchronization and asynchronous quenching of periodic oscillations in a thermoacoustic system. J. Fluid Mech. 864, 73–96 (2019)
- Coccolo, M., Seoane, J., Lenci, S., Sanjuán, M.: Fractional damping effects on the transient dynamics of the duffing oscillator. Commun. Nonlinear Sci. Numer. Simul. 117, 106959 (2023)
- Ghosh, A., Mondal, S., Sujith, R.: Occasional coupling enhances amplitude death in delay-coupled oscillators. Chaos 32(10), 101106 (2022)
- Ghosh, A., Chakraborty, S.: Comprehending deterministic and stochastic occasional uncoupling induced synchronizations through each other. Eur. Phys. J. B 93(6), 113 (2020)
- 22. Thomas, N., Mondal, S., Pawar, S., Sujith, R.: Effect of timedelay and dissipative coupling on amplitude death in coupled thermoacoustic oscillators. Chaos **28**(3), 033119 (2018)



 Thomas, N., Mondal, S., Pawar, S., Sujith, R.: Effect of noise amplification during the transition to amplitude death in coupled thermoacoustic oscillators. Chaos 28(9), 093116 (2018)

- Biwa, T., Tozuka, S., Yazaki, T.: Amplitude death in coupled thermoacoustic oscillators. Phys. Rev. Appl. 3(3), 034006 (2015)
- Hyodo, H., Biwa, T.: Stabilization of thermoacoustic oscillators by delay coupling. Phys. Rev. E 98(5), 052223 (2018)
- Zheng, L., Liao, Y., Kim, K., Zhou, J., Guan, Y.: Amplitude death in ring-coupled network with asymmetric thermoacoustic oscillators and nonlocal time-delay interactions. Nonlinear Dyn. 113(7), 6141–6156 (2025)
- Coccolo, M., Zhu, B., Sanjuán, M., Sanz-Serna, J.: Bogdanov–Takens resonance in time-delayed systems. Non-linear Dyn. 91(3), 1939–1947 (2018)
- Guan, Y., Murugesan, M., Li, L.: Strange nonchaotic and chaotic attractors in a self-excited thermoacoustic oscillator subjected to external periodic forcing. Chaos 28(9), 093109 (2018)
- Guan, Y., Li, L., Ahn, B., Kim, K.: Chaos, synchronization, and desynchronization in a liquid-fueled diffusion-flame combustor with an intrinsic hydrodynamic mode. Chaos 29(5), 053124 (2019)
- Guan, Y., Gupta, V., Li, L.: Intermittency route to selfexcited chaotic thermoacoustic oscillations. J. Fluid Mech. 894, 3 (2020)
- Coccolo, M., Cantisán, J., Seoane, J., Rajasekar, S., Sanjuán, M.: Delay-induced resonance suppresses dampinginduced unpredictability. Phil. Trans. R. Soc. A 379(2192), 20200232 (2021)
- Cantisán, J., Coccolo, M., Seoane, J., Sanjuán, M.: Delayinduced resonance in the time-delayed duffing oscillator. Int. J. Bifurc. Chaos 30(03), 2030007 (2020)
- Ortiz, A., Yang, J., Coccolo, M., Seoane, J., Sanjuán, M.: Fractional damping enhances chaos in the nonlinear Helmholtz oscillator. Nonlinear Dyn. 102(4), 2323–2337 (2020)
- McManus, K., Poinsot, T., Candel, S.: A review of active control of combustion instabilities. Prog. Energy Combust. Sci. 19(1), 1–29 (1993)
- Candel, S.: Combustion dynamics and control: progress and challenges. Proc. Combust. Inst. 29(1), 1–28 (2002)
- Poinsot, T.: Prediction and control of combustion instabilities in real engines. Proc. Combust. Inst. 36(1), 1–28 (2017)
- Bellows, B., Hreiz, A., Lieuwen, T.: Nonlinear interactions between forced and self-excited acoustic oscillations in premixed combustor. J. Propul. Power 24(3), 628–631 (2008)
- Cosić, B., Bobusch, B., Moeck, J., Paschereit, C.: Open-loop control of combustion instabilities and the role of the flame response to two-frequency forcing. J. Eng. Gas Turbines Power 134(6), 061502 (2012)
- Guan, Y., He, W., Murugesan, M., Li, Q., Liu, P., Li, L.: Control of self-excited thermoacoustic oscillations using transient forcing, hysteresis and mode switching. Combust. Flame 202, 262–275 (2019)
- Wang, P., Tian, Y., Yang, L., Luo, S., Li, J., Liu, T.: Openloop control of thermoacoustic instabilities by the external acoustic forcing at different frequencies. Proc. Combust. Inst. 40(1–4), 105540 (2024)
- Liao, Y., Choi, Y., Liu, P., Kim, K., Guan, Y.: Active control of thermoacoustic instability in a lean-premixed hydrogen-

- enriched combustor via open-loop acoustic forcing. Combust. Flame **277**, 114175 (2025)
- Guan, Y., Gupta, V., Wan, M., Li, L.: Forced synchronization of quasiperiodic oscillations in a thermoacoustic system. J. Fluid Mech. 879, 390–421 (2019)
- Guan, Y., Yin, B., Yang, Z., Li, L.: Forced synchronization of self-excited chaotic thermoacoustic oscillations. J. Fluid Mech. 982, 9 (2024)
- Juniper, M.: Triggering in the horizontal Rijke tube: nonnormality, transient growth and bypass transition. J. Fluid Mech. 667, 272–308 (2011)
- Magri, L., Juniper, M.: Sensitivity analysis of a time-delayed thermo-acoustic system via an adjoint-based approach. J. Fluid Mech. 719, 183–202 (2013)
- Srikanth, S., Sahay, A., Pawar, S., Manoj, K., Sujith, R.: Self-coupling: an effective method to mitigate thermoacoustic instability. Nonlinear Dyn. 110(3), 2247–2261 (2022)
- Doranehgard, M., Gupta, V., Li, L.: Quenching and amplification of thermoacoustic oscillations in two nonidentical Rijke tubes interacting via time-delay and dissipative coupling. Phys. Rev. E 105(6), 064206 (2022)
- 48. King, L.: XII. On the convection of heat from small cylinders in a stream of fluid: determination of the convection constants of small platinum wires with applications to hot-wire anemometry. Philos. Trans. R. Soc. Lond. A 214(509–522), 373–432 (1914)
- Heckl, M.: Non-linear acoustic effects in the Rijke tube.
   Acta Acust. United Acoust. 72(1), 63–71 (1990)
- Zinn, B., Lores, M.: Application of the Galerkin method in the solution of non-linear axial combustion instability problems in liquid rockets. Combust. Sci. Technol. 4(1), 269–278 (1971)
- Balasubramanian, K., Sujith, R.: Thermoacoustic instability in a Rijke tube: non-normality and nonlinearity. Phys. Fluids 20(4), 044103 (2008)
- Matveev, K.: Thermoacoustic Instabilities in the Rijke Tube: Experiments and Modeling. California Institute of Technology, Pasadena (2003)
- Guan, Y., Gupta, V., Kashinath, K., Li, L.: Open-loop control of periodic thermoacoustic oscillations: experiments and low-order modelling in a synchronization framework. Proc. Combust. Inst. 37(4), 5315–5323 (2019)
- Keen, B., Fletcher, W.: Suppression of a plasma instability by the method of "asynchronous quenching". Phys. Rev. Lett. 24(4), 130 (1970)
- Ohe, K., Takeda, S.: Asynchronous quenching and resonance excitation of ionization waves in positive columns. Contrib. Plasma Phys. 14(2), 55–65 (1974)
- Pikovsky, A., Rosenblum, M., Kurths, J.: Synchronization: A Universal Concept in Nonlinear Sciences. Cambridge Nonlinear Science Series, Cambridge University Press, Cambridge (2001)
- Li, L., Juniper, M.: Lock-in and quasiperiodicity in a forced hydrodynamically self-excited jet. J. Fluid Mech. 726, 624– 655 (2013)
- Guan, Y., Li, L., Jegal, H., Kim, K.: Effect of flame response asymmetries on the modal patterns and collective states of a can-annular lean-premixed combustion system. Proc. Combust. Inst. 39(4), 4731–4739 (2023)
- Guan, Y., Choi, Y., Liu, P., Kim, K.: Mutual synchronization and flame dynamics in an axially fuel-staged lean-premixed



- combustion system. Proc. Combust. Inst. **40**(1–4), 105197 (2024)
- Latour, V., Durox, D., Renaud, A., Candel, S.: Experiments on symmetry breaking of azimuthal combustion instabilities and their analysis combining acoustic energy balance and flame describing functions. J. Fluid Mech. 985, 31 (2024)
- Qin, L., Wang, X., Zhang, G., Sun, X.: Suppression of azimuthal combustion instability using perforated liner under symmetry breaking. J. Propul. Power 41(1), 27–39 (2025)
- Shampine, L., Thompson, S.: Solving DDEs in MATLAB. Appl. Numer. Math. 37(4), 441–458 (2001)
- Daw, C., Kennel, M., Finney, C., Connolly, F.: Observing and modeling nonlinear dynamics in an internal combustion engine. Phys. Rev. E 57(3), 2811 (1998)
- Bonciolini, G., Faure-Beaulieu, A., Bourquard, C., Noiray, N.: Low order modelling of thermoacoustic instabilities and intermittency: flame response delay and nonlinearity. Combust. Flame 226, 396–411 (2021)

 Burnley, V., Culick, F.: Influence of random excitations on acoustic instabilities in combustion chambers. AIAA J. 38(8), 1403–1410 (2000)

**Publisher's Note** Springer Nature remains neutral with regard to jurisdictional claims in published maps and institutional affiliations.

